Herschel GASPS spectral observations of T Tauri stars in Taurus. Unraveling far-infrared line emission from jets and discs

Alonso-Martínez, M.; Riviere-Marichalar, P.; Meeus, G.; Rentzsch-Holm, Inga; Fang, M.; Podio, L.; Dent, W. R. F.; Eiroa, C.

Published in:
Astronomy & Astrophysics

DOI:
10.1051/0004-6361/201629005

Publication date:
2017

A&A 603, A138 (2017)
DOI: 10.1051/0004-6361/201629005

Astronomy & Astrophysics

Herschel GASPS spectral observations of T Tauri stars in Taurus

Unraveling far-infrared line emission from jets and discs⋆

M. Alonso-Martínez[1,2], P. Riviere-Marichalar[1,3], G. Meeus[1,2], I. Kamp[4], M. Fang[1,5], L. Podio[6], W. R. F. Dent[7], and C. Eiroa[1,2]

[1] Dpto. de Física Teórica, Fac. de Ciencias, UAM Campus Cantoblanco, 28049 Madrid, Spain
e-mail: miguel.alonso@uam.es
[2] Astro-UAM, UAM, Unidad Asociada CSIC, 28049 Madrid, Spain
[3] Dpto. de Astrofísica, Centro de Astrobiología, ESAC Campus, PO Box 78, 28691 Villanueva de la Cañada, Madrid, Spain
[4] Kapteyn Astronomical Institute, University of Groningen, Postbus 800, 9700 AV Groningen, The Netherlands
[5] Department of Astronomy, University of Arizona, 933 North Cherry Avenue, Tucson, AZ 85721, USA
[6] INAF–Osservatorio Astrofisico di Arcetri, Largo E. Fermi 5, 50125 Firenze, Italy
[7] ALMA SCO, Alonso de Cordova 3107, Vitacura 763-0355, Santiago, Chile

Received 26 May 2016 / Accepted 14 March 2017

ABSTRACT

Context. At early stages of stellar evolution young stars show powerful jets and/or outflows that interact with protoplanetary discs and their surroundings. Despite the scarce knowledge about the interaction of jets and/or outflows with discs, spectroscopic studies based on *Herschel* and ISO data suggests that gas shocked by jets and/or outflows can be traced by far-IR (FIR) emission in certain sources.
Aims. We want to provide a consistent catalogue of selected atomic ([OI] and [CII]) and molecular (CO, H_2O, and OH) line fluxes observed in the FIR, separate and characterize the contribution from the jet and the disc to the observed line emission, and place the observations in an evolutionary picture.
Methods. The atomic and molecular FIR (60–190 μm) line emission of protoplanetary discs around 76 T Tauri stars located in Taurus are analysed. The observations were carried out within the *Herschel* key programme Gas in Protoplanetary Systems (GASPS). The spectra were obtained with the Photodetector Array Camera and Spectrometer (PACS). The sample is first divided in outflow and non-outflow sources according to literature tabulations. With the aid of archival stellar/disc and jet/outflow tracers and model predictions (PDRs and shocks), correlations are explored to constrain the physical mechanisms behind the observed line emission.
Results. Outflow sources exhibit brighter atomic and molecular emission lines and higher detection rates than non-outflow sources. The line detection fractions decrease with SED evolutionary status (from Class I to Class III). We find correlations between [OI] 63.18 μm and [OI] 6300 Å, o-H_2O 78.74 μm, CO 144.78 μm, OH 79.12+79.18 μm, and the continuum flux at 24 μm. The atomic line ratios can be explain either by fast ($V_{\rm shock} > 50$ km s^{-1}) dissociative J-shocks at low densities ($n \sim 10^3$ cm^{-3}) occurring along the jet and/or PDR emission ($G_0 > 10^2$, $n \sim 10^3$–10^6 cm^{-3}). To account for the [CII] absolute fluxes, PDR emission or UV irradiation of shocks is needed. In comparison, the molecular emission is more compact and the line ratios are better explained with slow ($V_{\rm shock} < 40$ km s^{-1}) C-type shocks with high pre-shock densities (10^4–10^6 cm^{-3}), with the exception of OH lines, that are better described by J-type shocks. Disc models alone fail to reproduce the observed molecular line fluxes, but a contribution to the line fluxes from UV-illuminated discs and/or outflow cavities is expected. Far-IR lines dominate disc cooling at early stages and weaken as the star+disc system evolves from Class I to Class III, with an increasing relative disc contribution to the line fluxes.
Conclusions. Models which take into account jets, discs, and their mutual interaction are needed to disentangle the different components and study their evolution. The much higher detection rate of emission lines in outflow sources and the compatibility of line ratios with shock model predictions supports the idea of a dominant contribution from the jet/outflow to the line emission, in particular at earlier stages of the stellar evolution as the brightness of FIR lines depends in large part on the specific evolutionary stage.

Key words. stars: formation – circumstellar matter – protoplanetary disks – stars: evolution – astrochemistry – stars: jets

1. Introduction

Protoplanetary discs are ubiquitously found around young stars and are the birth sites of planets. They are initially composed of well-mixed gas and dust (e.g. Williams & Cieza 2011, and references therein) and are in continuous evolution (e.g. Semenov 2011). Although gas constitutes the bulk of the disc mass, before the advent of ALMA our knowledge of protoplanetary discs was mainly based on dust studies (e.g. Beckwith et al. 1990; Andrews & Williams 2005; Hartmann 2008).

Different molecular transitions probe a diversity of gas kinetic temperatures and densities; for example, CO ro-vibrational transitions can be excited in hot ($T \sim 4000$ K) and dense ($n > 10^{10}$ cm^{-3}) gas located at ~1 au (e.g. Hamann et al. 1988), whereas purely rotational transitions are excited at much lower temperatures (typically a few hundred) beyond 1 au (Najita et al. 2003). The mid-IR observations of molecular lines (H_2 and CO) and forbidden atomic and ionized lines (S and Fe) trace warm gas ($T \sim 50$–100 K) at a few radii from the central star up to several tens of au (Pascucci et al. 2006). In the submillimetre,

⋆ *Herschel* is an ESA space observatory with science instruments provided by European-led Principal Investigator consortia and with important participation from NASA.

CO observations (Piétu et al. 2007), as well as HCO^+, H_2CO, HCN, and CN (e.g. Öberg et al. 2011, and references therein), probe cold gas (20 K < T < 50 K) at radii >20 au. The incident radiation field, depth in the disc, and distance from the central star, etc., govern the chemical reactions and temperature structure of the gas in protoplanetary discs (Dutrey et al. 2014).

Young stars produce X-ray and far-ultraviolet (FUV) radiation (Calvet et al. 2004; Ingleby et al. 2013) either by chromospheric activity (Robrade et al. 2007) or by accretion (Güdel et al. 2007b). This radiation shapes the structure of the disc and its temperature distribution. In the inner 50 au of the disc surface, the temperature can be up to $\sim 10^4$ K (Jonkheid et al. 2004; Kamp & Dullemond 2004), favouring a rich ion–atomic chemistry, while in deeper and colder (~100 K) regions where the UV/X-ray photons can still penetrate, the chemistry is more ion–molecule rich. Determination of where the different lines arise gives insight on accretion, photoevaporation, and planet formation mechanisms (Frank et al. 2014, and references therein).

Jets, outflows, and winds associated with young stellar objects have been observed from X-ray to radio wavelengths (Hartigan et al. 1995; Reipurth & Bally 2001; Bally et al. 2007; Schneider et al. 2013; Lynch et al. 2013) in scales that range from tens of au (Agra-Amboage et al. 2011) up to several parsecs (McGroarty et al. 2004), and can persist for millions of years (Cabrit et al. 2011). The *Herschel* Space Observatory (HSO; Pilbratt et al. 2010) has revealed that, on average, far-IR (FIR) emission lines are more frequently seen and are stronger in systems with jets and/or outflows (e.g. Podio et al. 2012; Howard et al. 2013; Lee et al. 2014) with temperatures of ~100–1000 K (Karska et al. 2014b). Traditionally, the role played by jet/outflows and protoplanetary discs in stellar evolution is treated separately, although shocks produced by a jet are important contributors to emission; hence, they affect the chemical properties of the disc.

The Gas in Protoplanetary Systems (GASPS; Mathews et al. 2010; Dent et al. 2013) programme observed 240 stars in different star forming regions in order to probe the evolution of gas and dust in protoplanetary discs. The *Herschel*/PACS (Photodetector Array Camera and Spectrometer, Poglitsch et al. 2010) was used to observe 76 T Tauri stars in the Taurus region. Howard et al. (2013) concentrated on [OI] 63.18 μm, but also listed line intensities for [OI] 145.53 μm and [CII] 157.74 μm and identified other lines in the spectra. Riviere-Marichalar et al. (2012) analysed the o-H_2O 63.32 μm line; Keane et al. (2014) focused on [OI] 63.18 μm and o-H_2O 63.32 μm lines in transitional discs; and Podio et al. (2012) focused on the analysis of six well-known jet sources showing extended [OI] 63.18 μm emission.

In this work, we make an inventory of atomic and molecular species covered with PACS in the Taurus sample, and present a consistent line flux catalogue. We assess whether the observed emission is dominated by the jet or the disc, and how this depends on the evolutionary status of the source. Observations include atomic [OI] and [CII], and molecular H_2O, CO, and OH. These lines have been attributed to arise in discs in TW Hya (Kamp et al. 2013), HD 163296 (Tilling et al. 2012) and HD 100546 (Thi et al. 2011). Indeed disc models (e.g. the DENT grid Woitke et al. 2010; Pinte et al. 2010; Kamp et al. 2011) can reproduce the line ratios but fail to explain high line fluxes. In addition, FIR line emission with a jet/outflow origin has been spatially resolved for several Class 0/I protostars clearly showing that the line emission is more extended than continuum emission (Herczeg et al. 2012).

The structure of the paper is as follows. Section 2 describes the sample and observations. The data reduction is explained in Sect. 3, and the main results are described in Sect. 4. Relations between FIR lines are explored in Sect. 5, and its possible origins and excitation mechanisms are discussed in Sect. 6. The main conclusions are summarized in Sect. 7.

2. Sample and observations

2.1. The sample

The sample consists of 76 T Tauri stars of the Taurus region observed by GASPS. Spectral types, as given by Luhman et al. (2010) and Herczeg & Hillenbrand (2014), range from K0 to M6, except for three earlier type stars: RY Tau (G0), SU Aur (G4), and HD 283573 (G4). More than one-third of the stars in the sample (~38%) are multiple systems (Ghez et al. 1993; Daemgen et al. 2015), with separations from 0.1 up to 6 arcsec (14–840 au). In these cases, the companions can contaminate the *Herschel*/PACS results since the pixel size is 9.4 arcsec, corresponding to a separation of ~1300 au at the distance of Taurus (140 pc). However, we kept those binary sources in our sample in order not to bias the results (see Sect. 5.5 in Howard et al. 2013, for a discussion).

Following the classification by Lada (1987), the sample includes 5 Class I, 55 Class II (including 10 transition discs; Strom et al. 1989; Najita et al. 2007), and 16 Class III objects. The SED classification is taken from Luhman et al. (2010) and/or Rebull et al. (2010). Objects not observed by these authors and with no sign of infrared excess are classified as Class III. The sample is divided in outflow and non-outflow sources motivated by the correlation between the 63/70 μm continuum emission and the [OI] 63.18 μm line flux in Taurus and Chamaelon II stars found by Howard et al. (2013) and Riviere-Marichalar et al. (2014). The outflow sources are those showing blue-shifted [OI] 6300 Å emission in Hartigan et al. (1995). A more detailed description of the sample is given in Table A.1, including stellar temperatures, mass accretion rates, stellar X-ray and accretion luminosities, ages, and disc masses.

2.2. Herschel/PACS observations

Spectroscopic observations were performed between February 2010 and March 2012. PACS covers the wavelength range 51–220 μm in two channels (blue: 51–105 μm and red: 102–220 μm). The spatial resolution of the PACS spectrometer is 9.4″ at 62–100 μm, 11.4″ at 150 μm and 13.1″ at 180 μm. The integral field unit (IFU) images a 47″ × 47″ field of view (FOV) in 5 × 5 spatial pixels (hereafter spaxels) of 9.4″ × 9.4″ each. For each spaxel, two spectra are obtained simultaneously, one for each channel.

The observations were conducted in chop-nod line (LineSpec) and range (RangeSpec) modes (see Chapt. 6.2.6 of the PACS Observers Manual) with a small throw (1.5′) to remove telescope and background emission. The observations were performed in one (1152 s on source) or two (3184 s on source) nod cycles with total integration times in the range ~1250–6630 s and ~5140–20 555 s for LineSpec and RangeSpec modes, respectively. The LineSpec mode has a small wavelength coverage (62.93–63.43 μm) targeting the [OI] 63.18 μm and o-H_2O 63.32 μm lines and the adjacent continuum. The RangeSpec observations cover a larger wavelength range, defined by the observer. The lines observed in this mode include

Table 1. Observed wavelength ranges, resolution, instrument configuration, amount of sources observed, and properties of the main transitions covered.

Channel	$\lambda\lambda$ [μm]	R	Mode	No. Sources	Sp	Transition	T_{ex} [K]	λ_0 [μm]
Blue	62.93–63.43	3150	LineSpec	76	[OI]	$^3P_1$–$^3P_2$	228	63.18
					o-H_2O	8_{18}–7_{07}	1293	63.32
Red	188.76–190.29	1500	LineSpec	76	DCO^+	J = 22–21	2068	189.57
Blue	71.82–73.33	1800	RangeSpec	39	o-H_2O	7_{07}–6_{16}	685	71.94
					CH^+	J = 5–4	600	72.14
					CO	J = 36–35	3700	72.84
Red	143.61–146.66	1200	RangeSpec	39	p-H_2O	4_{13}–3_{22}	396	144.52
					CO	J = 18–17	945	144.78
					[OI]	$^3P_0$–$^3P_1$	326	145.52
Blue	78.37–79.73	1900	RangeSpec	38	o-H_2O	4_{23}–3_{12}	432	78.74
					p-H_2O	6_{15}–5_{24}	396	78.92
					OH	$^2\Pi_{1/2,1/2}$–$^2\Pi_{3/2,3/2}$	182	79.12+79.18
					CO	J = 33–32	3092	79.36
Red	156.73–159.43	1250	RangeSpec	38	[CII]	$^2P_{3/2}$–$^2P_{1/2}$	91	157.74
					p-H_2O	3_{31}–4_{04}	410	158.31
Blue	89.29–90.72	2500	RangeSpec	30	p-H_2O	3_{22}–2_{11}	297	89.99
					CO	J = 29–28	2400	90.16
Red	178.58–181.44	1450	RangeSpec	30	o-H_2O	2_{12}–1_{01}	115	179.53
					o-H_2O	2_{21}–2_{12}	194	180.49

several transitions of o-H_2O (at 71.94, 78.74, 179.53, and 180.49 μm), p-H_2O (at 78.92, 89.99, and 144.52 μm), CO (at 72.74, 79.36, 90.16, and 144.78 μm), and a OH doublet (at 79.12 and 79.18 μm). The entire sample (76 sources) was observed in LineSpec mode, while for the RangeSpec mode the number of targets observed varies. None of the RangeSpec observations includes Class III objects. Details of the instrument channel, coverage, spectral resolution, observing mode, number of observed sources, and emission lines covered are summarized in Table 1. Identifiers (OBSIDs) and exposure times of the spectroscopic observations are summarized in Table B.1.

3. Data reduction

The data were reduced using HIPEv10 (Ott 2013). The PACS pipeline removes saturated and bad pixels, subtracts the chop on and the chop off nod positions, applies a correction for the spectral response function and flat field, and re-bins at half the instrumental resolution (oversample = 2, upsample = 1). The final spectrum is obtained by the average of the two nod cycles. The spaxel showing the highest continuum level is extracted and an aperture correction applied. To estimate the continuum flux, the noisy edges of the spectra are removed, as are $\pm 3\sigma$ regions around each line present in the spectral range of interest. Then, a first-order polynomial fit is applied. The line fluxes are obtained from the continuum subtracted spectra by Gaussian fits to the lines, and considered as real when the signal-to-noise ratio of the emission peak is $>3\sigma$. The errors in line fluxes are computed as the integral of a Gaussian with width equal to the fitted value, and peak equal to the RMS noise of the continuum. In case of non-detections, we report 3σ upper limits computed as the integral of a Gaussian with a FWHM equal to the instrumental $FWHM_0$ at the wavelength of interest, and amplitude three times the standard deviation of the continuum. The line fluxes and upper limits in the 60–80 μm and 90–190 μm ranges are given in Tables C.1 and C.2, respectively.

There are a few problems with our approach of only extracting the spaxel with the highest continuum level, as described below. In most cases, the fluxes were extracted from the central spaxel at the location of the star. However, some Taurus observations suffer from large pointing errors, which means that the star lies between two or more spaxels; in these cases the reported fluxes are lower limits to the real flux. Previous papers have tried to solve this problem either by reconstructing the PSF to recover the on-source emission (Howard et al. 2013) or by integrating all the spaxels (5×5) to recover the extended emission (Podio et al. 2012). An intermediate solution that we apply is to derive the flux by summing the 3×3 spaxels around the position of the source. When the difference in flux is larger than three times the quadratic sum of the errors, the 3×3 fluxes are considered more accurate. In these cases, the 3×3 fluxes are used instead of the fluxes extracted from a single spaxel. These are listed in Tables C.3 and C.4. For the jet sources showing [OI] 63.18 μm extended emission, we obtained lower line fluxes than those given in Podio et al. (2012).

Figure 1 compares the [OI] 63.18 μm line flux with those published in Howard et al. (2013) and Keane et al. (2014) and the o-H_2O 63.32 μm in Riviere-Marichalar et al. (2012). These three studies used different HIPE versions to reduce the data, but similar line fitting algorithms to estimate line fluxes. The main discrepancies are towards extended, misaligned objects or towards objects displaying very high [OI] fluxes (above $\sim 10^{-16}$ W m^{-2}). For these observations the median differences are between 11% and 27%, compatible with the PACS absolute flux accuracy (see pages 40–44 of PACS Observers' Manual). More recent pipeline versions (HIPEv14) aim to recover the emission from mispointed sources. A comparative test yields that fluxes from the different HIPE versions are compatible within errors.

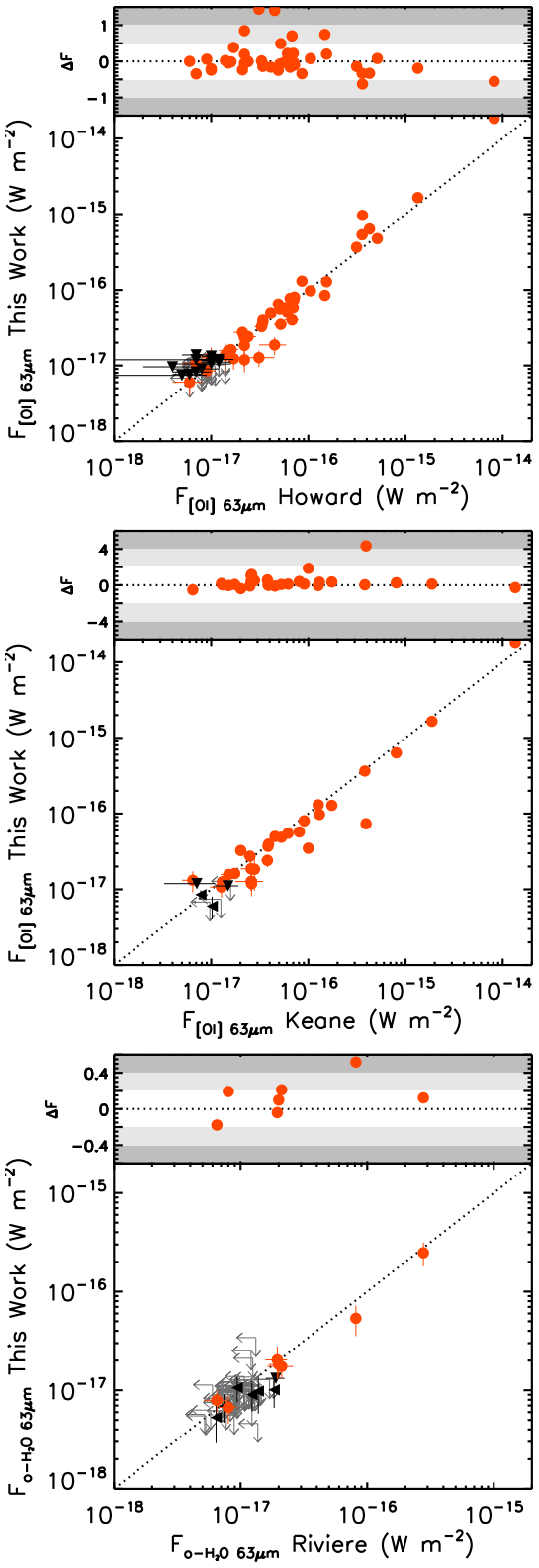

Fig. 1. Comparison of our [OI] 63.18 μm fluxes with those in Howard et al. (2013; *top*) and Keane et al. (2014; *middle*), and comparison of o-H_2O 63.32 μm fluxes with those in Riviere-Marichalar et al. (2012; *bottom*). In all the panels the red circles represent the detections, while black down-facing and left-facing triangles are upper limits in the y-axis and x-axis, respectively. Arrows represent upper limits in both axes. ΔF ($\frac{F_{\rm old}-F_{\rm new}}{F_{\rm new}}$) is the fractional difference between the two sets of measurements.

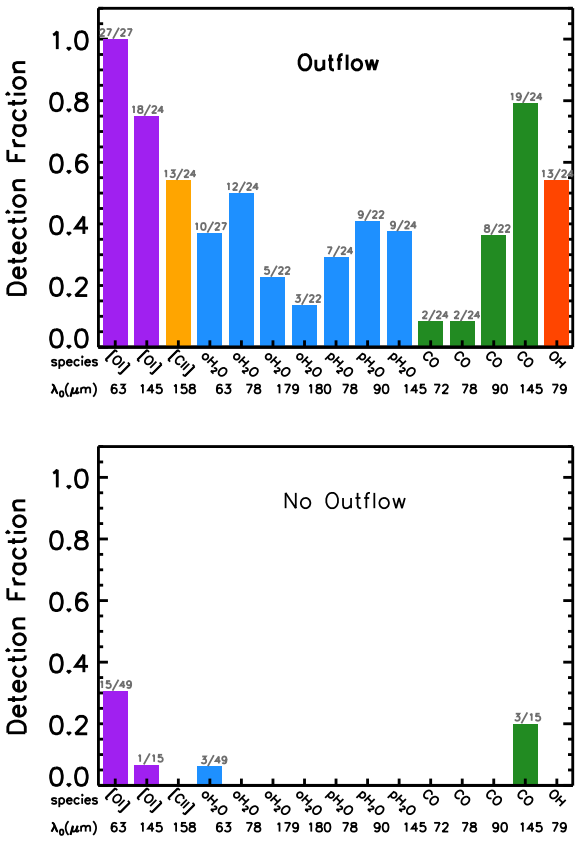

Fig. 2. Line emission detection fractions for the different species observed within PACS range. Objects with (*top*) and without (*bottom*) an outflow. Each species has a different colour: [OI] (purple), [CII] (yellow), H_2O (blue), CO (green), and OH (red). The numbers on top of the bars refer to the total detections over the total targets observed. The atomic/molecular species and central wavelengths for the transitions are also indicated.

4. Results

Atomic ([OI] and [CII]) and molecular (CO, H_2O, and OH) emission lines are seen in a large number of Taurus sources. Table D.1 gives the detection fractions for the entire sample, as well as the split in outflow and non-outflow sources. Uncertainties were estimated assuming binomial distributions (see Burgasser et al. 2003). A clear result (Fig. 2) is that outflow sources are richer in emission lines, and show systematically higher fluxes (on average $\sim 10^{-16}$ W m^{-2} compared to $\sim 10^{-17}$ W m^{-2}) and detection fractions (on average 42% compared to 16%) than non-outflow sources.

This suggests that jets and/or outflows are important contributors to the line emission and that they dominate in sources showing extended emission (Podio et al. 2012). However, a (partial) disc origin cannot be ruled out. In the following we discuss the atomic and molecular line detections in more detail according to outflow activity, evolutionary status, and spectral types.

4.1. Atomic emission lines

4.1.1. [OI] emission

Figures 3 and 4 show spectra centred on the [OI] fine-structure lines at 63.18 and 145.53 μm. The [OI] 63.18 μm is detected in 42 out of 76 stars (55%); the line is detected towards all outflow sources, but for non-outflow sources

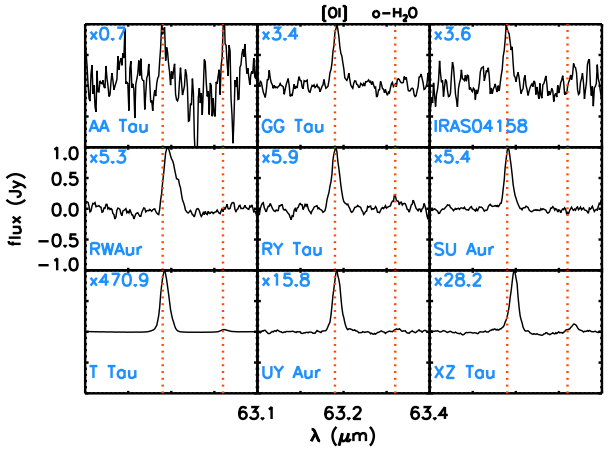

Fig. 3. Continuum subtracted spectra at 63 μm from the spaxel showing the highest continuum level. The scale is the same for all panels. The spectra were divided by the factor indicated in the upper left corner of each panel. The red lines indicate the position of the [OI] 63.18 μm and o-H_2O 63.32 μm lines. The offsets seen in the [OI] 63.18 μm line can be due to incorrect pointing or to the presence of an additional physical component.

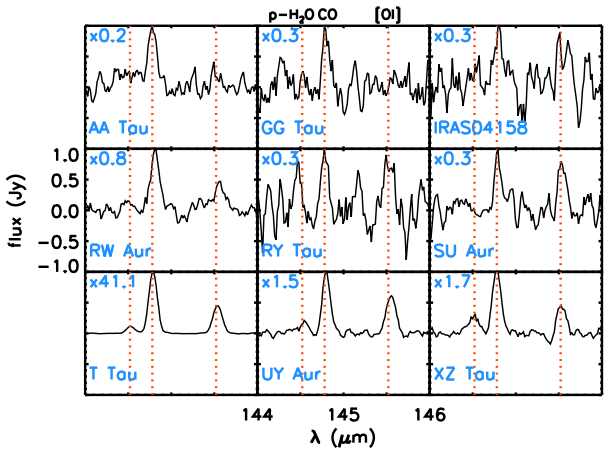

Fig. 4. Continuum subtracted spectra centred at 145 μm from the spaxel showing the highest continuum level. The scale is the same for all the panels. The spectra were divided by the factor indicated in the upper left corner of each panel. The red lines indicate the position of the p-H_2O 144.52 μm, CO 144.78 μm, and [OI] 145.53 μm lines.

the detection rate drops to 31%. Line fluxes vary between 6×10^{-18} and 2×10^{-14} W m^{-2}; outflows show stronger lines ($\sim 1 \times 10^{-17}$ – 2×10^{-14} W m^{-2}) than non-outflows ($\sim 6 \times 10^{-18}$–4×10^{-17} W m^{-2}). Unlike Howard et al. (2013), we did not detect [OI] 63.18 μm in CY Tau and Haro 6–37, probably due to different reduction pipelines and calibration files used. The profiles (see e.g. Fig. 3) are mainly Gaussians with some skewness in a few cases (e.g. XZ Tau). A recent and detailed study of [OI] 63.18 μm line profiles of young stellar objects (YSOs) by Riviere-Marichalar et al. (2016) suggests that such line profiles can be explained as a combination of disc, jet, and envelope emission.

Table D.2 shows the fraction of sources where the observed spectral lines are detected as a function of SED class. In the following, the statistics of Class II sources do not include transitional discs (TD). The atomic detection fractions decrease as the sources evolve from Class I down to Class III. The [OI] 63.18 μm line is detected in 100% of Class I objects, 70% of Class II objects, 60% of transitional discs, and 0% of Class III objects, with average fluxes decreasing from $\sim 3 \times 10^{-15}$ W m^{-2}, through $\sim 2 \times 10^{-16}$, to 3×10^{-17} W m^{-2} for Class I, Class II, and transitional discs respectively.

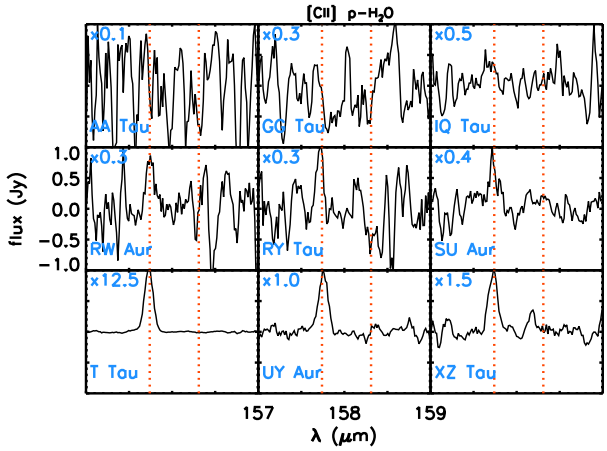

Fig. 5. Continuum subtracted spectra centred at 158 μm from the spaxel showing the highest continuum level. The scale is the same for all the panels. The spectra were divided by the factor in the upper left corner of each panel. The red lines indicate the position of the [CII] 157.74 μm and p-H_2O 158.31 μm lines.

Table D.3 gives the line detection fractions as a function of spectral types. The bins were selected so that they have a similar number of targets observed at 63 μm. For the [OI] 63.18 μm line, a decrease in the detection fraction with later spectral type is observed.

The [OI] 145.52 μm line is harder to excite than [OI] 63.18 μm because of its higher energy level (see T_{ex} in Table 1). Consequently, the line flux is on average ten times weaker than [OI] 63.18 μm. It is detected in 19 out of 39 objects (49%) with line fluxes between $\sim 10^{-18}$ W m^{-2} (the detection limit) and $\sim 8 \times 10^{-16}$ W m^{-2}. The detection rate is 75% (18 out of 24) for outflow sources, while it is only 7% (1 out of 15, DE Tau) for non-outflow objects. The fluxes decrease according to the evolutionary status of the source from $\sim 2 \times 10^{-16}$ W m^{-2} for Class I down to $\sim 3 \times 10^{-18}$ W m^{-2} for transitional discs.

4.1.2. [CII] emission

Some spectra centred at the [CII] 157.74 μm fine-structure line are shown in Fig. 5. We note that the [CII] line critical density is two orders of magnitude lower than for [OI] lines, making it easily excited in the surrounding cloud as well. In most of our targets the line is also detected in the *off*-source positions. The [CII] fluxes reported in Table C.2 are for the *on*- minus the *off*-positions to be consistent with the procedure followed for the rest of the lines.

The [CII] 157.74 μm emission line has a detection fraction of 34% (13 out of 38); only detected in 54% (13 out of 24) of the outflow sources with average line flux $\sim 7 \times 10^{-17}$ W m^{-2}. In DG Tau, DG Tau B, FS Tau, T Tau, UY Aur, and XZ Tau [CII] is observed as extended with an average line flux of $\sim 6 \times 10^{-17}$ W m^{-2}. RY Tau (TD) is associated with a jet, mapped in [OI] 6300 Å (Agra-Amboage et al. 2009), and embedded in diffuse and extended nebulosity (see Fig. 1 in St-Onge & Bastien 2008), suggesting that its [CII] line arises in its immediate surroundings.

We see a clear decline in the detection fractions from Class I (50%), through Class II (36%), to transitional discs (17%),

and average line fluxes of $\sim 2 \times 10^{-16}$, $\sim 4 \times 10^{-17}$, and $\sim 4 \times 10^{-18}$ W m^{-2}, respectively. This trend is similar to that observed for [OI] 63.18 μm.

4.2. Molecular emission lines

4.2.1. CO emission

Spectra of mid- to high-J CO transitions (see Table 1) are shown in Figs. 4–8. The CO J = 18–17 transition is most often detected in the stars observed (22 out of 39). Outflow sources have a detection rate of 79% (19 out of 24) with an average flux of $\sim 9 \times 10^{-17}$ W m^{-2}, while the line is only detected in 3 non-outflows sources (CI Tau, DE Tau, and HK Tau), i.e. a rate of 20% (3 out of 15) and an average flux of $\sim 3 \times 10^{-18}$ W m^{-2}. With respect to the SED classes, the detection fractions are 100% (4 out of 4) for Class I objects, decreasing to 59% (17 out of 29) for Class II objects, and 17% (1 out of 6) for transitional disc sources with average line fluxes of $\sim 3 \times 10^{-16}$, $\sim 2 \times 10^{-17}$, and $\sim 4 \times 10^{-18}$ W m^{-2}, respectively.

The CO J = 29–28, J = 33–32, and J = 36–35 lines are only detected in outflow sources, with detection fractions of 36% (8 out of 22), 8% (2 out of 24), and 8% (2 out of 24), respectively; their average line fluxes are $\sim 6 \times 10^{-17}$, $\sim 8 \times 10^{-17}$, and $\sim 6 \times 10^{-17}$ W m^{-2}, respectively. The J = 33–32 and J = 36–35 CO lines detections are in DG Tau (Class II) and T Tau (Class I/II), and are known to drive powerful bipolar jets (e.g. Eislöffel & Mundt 1998). None of the CO lines shows a trend with spectral type.

4.2.2. H_2O emission

Several transitions of water were observed (see Figs. 3, 4, 7–9). The o-H_2O lines at 78.74, 179.53, and 180.49 μm, and the p-H_2O lines at 78.92, 89.99, and 144.52 μm are only detected in outflow sources. The highest detection fraction is for o-H_2O 78.74 μm (50%) with an average $\sim 7 \times 10^{-17}$ W m^{-2}, followed by p-H_2O 89.99 μm (41%) and average flux of $\sim 5 \times 10^{-17}$ W m^{-2}. The p-H_2O 144.52 μm, 78.92 μm, o-H_2O 179.53, and 180.49 μm lines have respectively a detection fraction of 38%, 29%, 23%, and 14%; and average fluxes are of $\sim 2 \times 10^{-17}$, $\sim 2 \times 10^{-17}$, $\sim 1.4 \times 10^{-16}$, and $\sim 7 \times 10^{-17}$ W m^{-2}, respectively. The o-H_2O 63.32 μm line is detected in 10 out of 27 (37%) of the outflow sources with an average flux of $\sim 4 \times 10^{-17}$ W m^{-2}. It is the only water line detected in non-outflow sources, seen in 3 of them (6%), namely BP Tau, GI/GK Tau, and IQ Tau. This (*warm*) water line was first reported in Riviere-Marichalar et al. (2012), Fedele et al. (2013). The p-H_2O 158.31 μm line is undetected in all targets (even in T Tau). Table 2 lists the average water line fluxes of Class I, Class II, and TD sources. Water lines are brighter and more often detected (higher detection fractions) towards Class I objects than towards Class II and TD sources.

4.2.3. OH emission

Selected spectra of the hydroxyl doublet at 79.11 and 79.18 μm are shown in Fig. 8. The line is only detected in outflow sources (12 out of 38) with line flux values $\sim 10^{-16}$ W m^{-2}, on average. It is detected in 50% of the Class I sources (average flux $\sim 4 \times 10^{-16}$ W m^{-2}), decreasing to 38% in Class II (average flux $\sim 1.5 \times 10^{-17}$ W m^{-2}), and is undetected in transitional discs. We point out that DO Tau and DL Tau show peculiar OH detections: DO Tau shows only the 79.11 μm component, while DL Tau only shows the 79.18 μm component. We tested whether it could be due to significant pointing errors that translate into wavelength shifts which yield negative results (see Sect. 3.2.2 in Howard et al. 2013). Thus, the detection of only one component of the OH doublet appears to be real. Such asymmetries of OH lines in a doublet have already been noticed in ISO data (Goicoechea et al. 2011), in Class 0/I sources (Wampfler et al. 2013), and are discussed by Fedele et al. (2015) for HD 100546.

Table 2. Average water line fluxes at different wavelengths (60–180 μm) in units of 10^{-16} W m^{-2} for Class I, Class II, and TD objects.

Source	o-H_2O			
	63 μm	78 μm	179 μm	180 μm
Class I	1.05	2.50	6.35	2.05
Class II	0.10	0.14	0.20	0.07
TD	0.20	0.13	...	...
Source	**p-H_2O**			
	78 μm	90 μm	145 μm	158 μm
Class I	0.38	1.83	0.45	...
Class II	0.06	0.08	0.08	...
TD	...	0.10	0.04	...

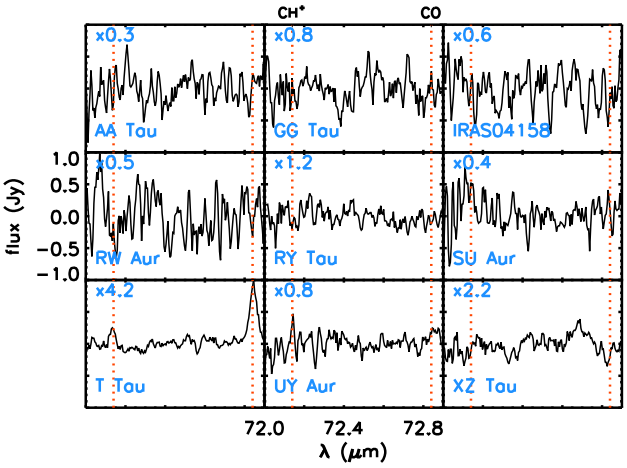

Fig. 6. Continuum subtracted spectra at 72 μm. The scale is the same for all the panels. The spectra were divided by the factor in the upper left corner of each panel. The red lines indicate the position of the CH^+ 72.14 μm and CO 72.84 μm lines.

4.2.4. CH^+ emission

The CH^+ feature remains undetected in almost all targets. Only T Tau shows CH^+ emission at 72.14 μm (see Fig. 6) with a line flux value of $1.77 \pm 0.65 \times 10^{-17}$ W m^{-2}. There could also be blends of CH^+ with H_2O lines at 89.99 and 179.53 μm.

5. Observational trends of far-IR lines

5.1. Evolution from Class 0/I to Class III

For the full sample of YSOs discussed here, the fraction of sources with [OI] 63.18 μm detections (55^{+5}_{-6}%) is higher than for older (>3 Myr) star forming regions like TW Hya (22%, age ~ 8–20 Myr; Riviere-Marichalar et al. 2013), Upper Sco (4%, age ~ 5–11 Myr; Mathews et al. 2013), Chapt. II (37%, age ~ 4 Myr; Riviere-Marichalar et al. 2014), and η Cha (8%, age ~ 5–9 Myr; Riviere-Marichalar et al. 2015). Such a decrease with age is a clear indication of evolution.

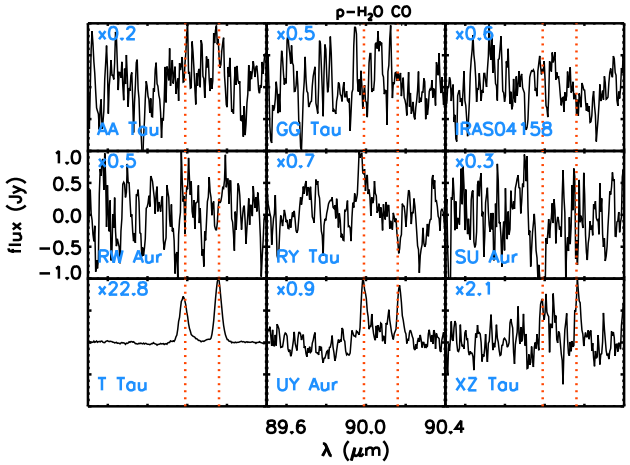

Fig. 7. Continuum subtracted spectra at 90 μm from the spaxel showing the highest continuum level. The scale is the same for all the panels. The spectra were divided by the factor in the upper left corner of each panel. The red lines indicate the position of the p-H_2O 89.99 μm and CO 90.16 μm lines.

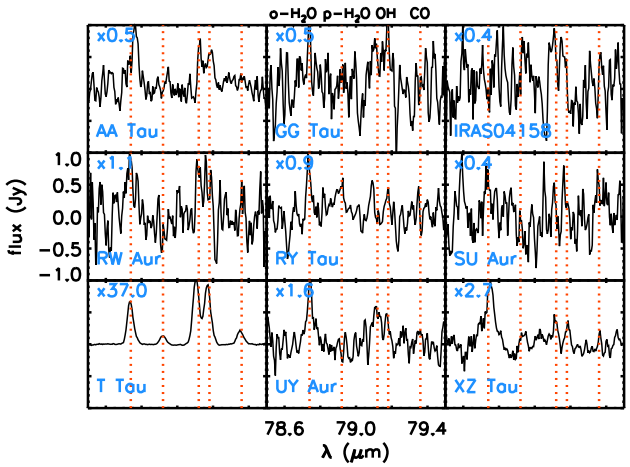

Fig. 8. Continuum subtracted spectra at 79 μm from the spaxel showing the highest continuum level. The scale is the same for all the panels. The spectra were multiplied by the factor in the upper left corner of each panel. The red lines indicate the position of the o-H_2O 78.74 μm line, p-H_2O 78.92 μm line, OH 79.11/79.18 μm doublet, and CO 79.36 μm lines.

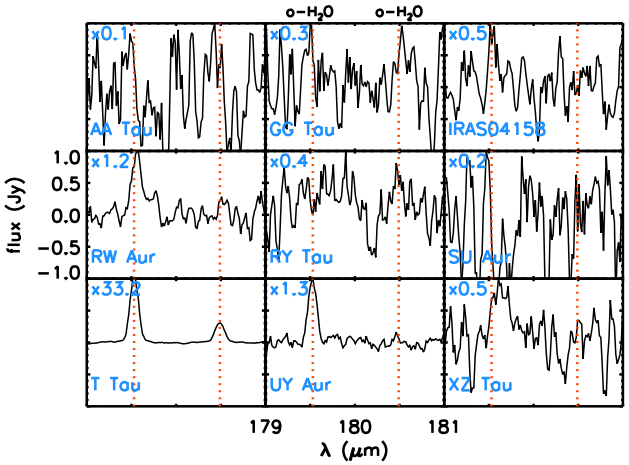

Fig. 9. Continuum subtracted spectra centred at 180 μm from the spaxel showing the highest continuum level. The scale is the same for all the panels. The spectra were divided by the factor in the upper left corner of each panel. The red lines indicate the position of the o-H_2O 179.53 and 180.49 μm lines.

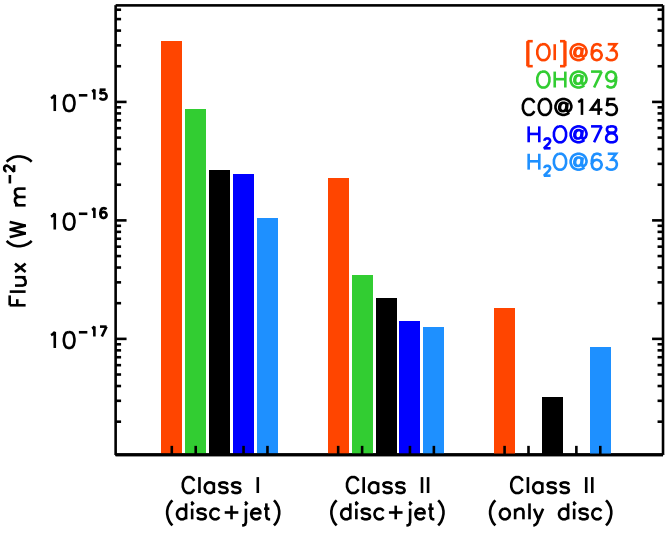

Fig. 10. Average line flux of [OI] 63.18 μm (red), OH 79.12+79.18 (green), CO 144.78 μm (black), o-H_2O 78.74 μm (dark blue), and o-H_2O 63.32 μm (blue) lines of Class I and II objects with jets and Class II sources with no jets. Most of the TD sources are included within Class II (only disc) objects. The exception is RY Tau (see Sect. 4.1), included in the Class II (disc+jet) group.

Figure 10 shows the average fluxes of the [OI] 63.18 μm, OH 79.12+79.18 μm, CO 144.78 μm, o-H_2O 78.74 μm, and o-H_2O 63.32 μm lines of Class I and II sources with jets, and for Class II objects with no jets, for which the OH 79.12+79.18 μm and o-H_2O at 78.74 μm lines are below the detection limit. The atomic and molecular line fluxes decrease rapidly, approximately by an order of magnitude at each stage, suggesting that a physical mechanism related to evolution is the most likely scenario.

One possible explanation could be that FIR line emission is due to a combination of jets shocking the surrounding material and UV radiation. In general, molecular emission from shocks is expected and is very important at the earliest stages, whereas photodissociation is more effective when the envelope dissipates (Nisini et al. 2002). In particular, H_2O in shocks is abundant because neutral-neutral reactions switch on at high temperature (see e.g. van Dishoeck et al. 2013). Processes involving dust grains are also important. Owing to photodesorption, sputtering, and grain-grain collisions, likely triggered by shocks, H_2O is also removed from icy dust grains. The progressive dissipation of gaseous and dusty envelopes from Class 0/I to Class III allows stellar or interstellar FUV fields to penetrate deeper and to dissociate more H_2O and OH to produce O. This scenario proposed by Nisini et al. (2002) was followed by Karska et al. (2013) to explain the FIR line weakening of CO and H_2O observed from Class 0 to Class I objects. When the mass accretion and outflow rates drop as the source evolves, the FIR emission originating in shock gas decrease because the strength of the FIR lines is related to the amount of shocked gas (Manoj et al. 2016). This does not hold for the more evolved Class II sources ("only disc" in Fig. 10), in which FIR line emission is coming from illuminated discs by UV (France et al. 2014) and X-ray (Güdel et al. 2007a). It is expected that as the disc is accreted and/or dispersed, the strength of the FIR lines will decrease too. This is also suggested by the non detections in Class III objects.

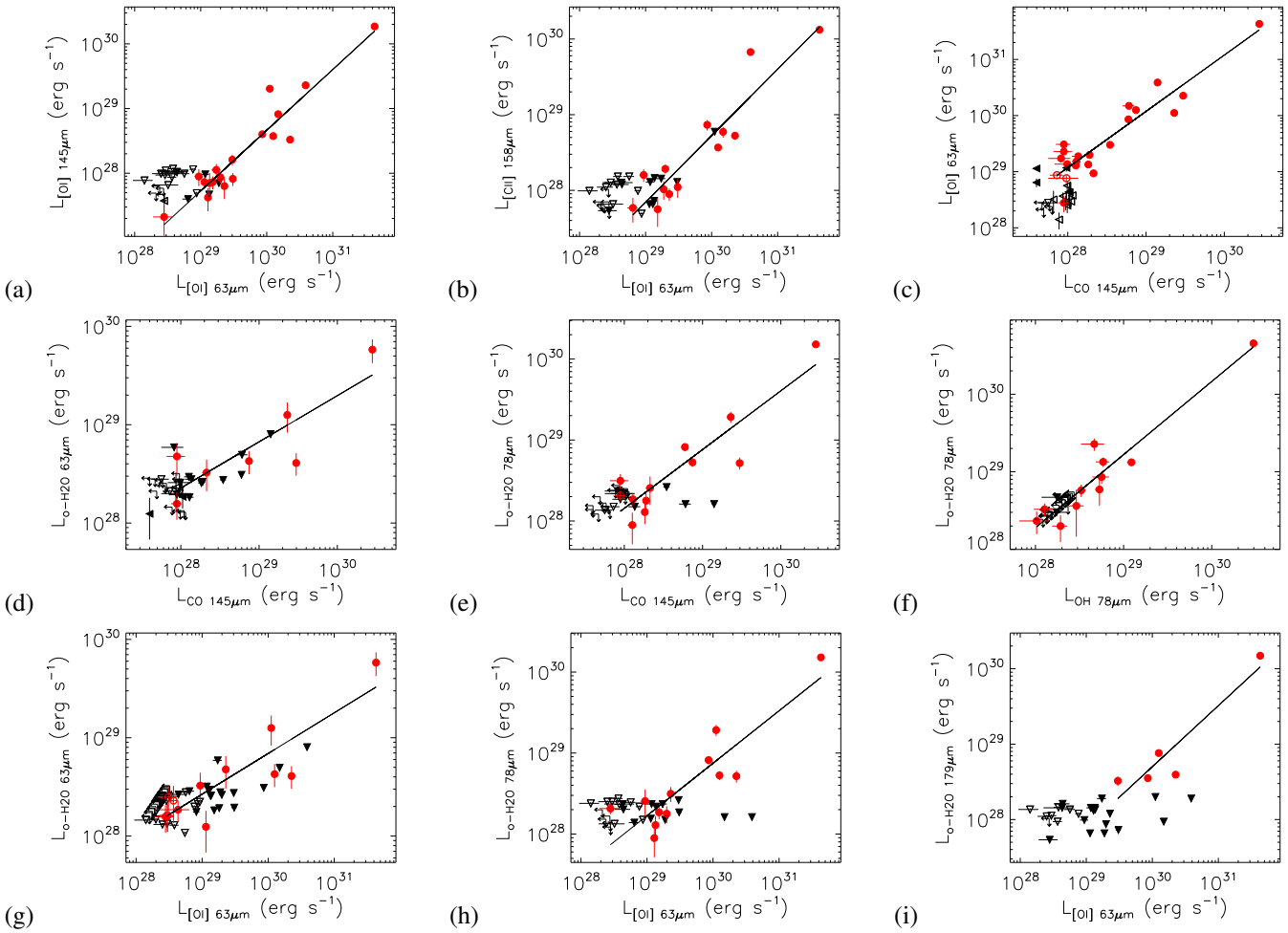

Fig. 11. Correlation plots between: **a)** [OI] 63.18 μm and [OI] 145.52 μm; **b)** [OI] 63.18 μm and [CII] 157.74 μm (see Howard et al. 2013); **c)** [OI] 63.18 μm and CO 144.78 μm; **d)** CO 144.78 μm and o-H_2O 63.32 μm; **e)** CO 144.78 μm and o-H_2O 78.74 μm; **f)** OH 79.12+79.18 μm and o-H_2O 78.74 μm; **g)** [OI] 63.18 μm and o-H_2O 63.32 μm (see Riviere-Marichalar et al. 2012); **h)** [OI] 63.18 μm and o-H_2O 78.74 μm; and **i)** [OI] 63.18 μm and o-H_2O 179.53 μm (tentatively). The red circles represent detections, grey triangles are upper limits in their pointing direction, and black arrows are upper limits in both axes. Filled symbols represent outflow sources. The solid line corresponds to a linear fit for detections.

5.2. Relations between far-IR lines

We performed an extensive search for correlations to address the possible origins of the FIR lines discussed here and to see how they are related. Only those atomic and molecular lines with high detection fractions were selected. Correlation factors $\rho_{x,y}$ (see Appendix A in Marseille et al. 2010), where (x, y) is the pair of lines considered, are used to validate any possible trends. The 3σ correlation corresponds to the threshold coefficient $\rho_{\rm thres} = 3/\sqrt{N-1}$, where N is the number of detections used in the calculation. Only those trends with correlation factors above the confidence threshold ($\rho_{\rm thres}$) are taken as statistically real: $|\rho| < 0.8$ denotes a lack of correlation, $0.8 < |\rho| < 0.9$ a weak (3σ) correlation, and $|\rho| > 0.9$ a strong correlation. To rule out that T Tau is somehow driving the correlations due to its high line fluxes (up to 200 times the median), the analysis is repeated without this star.

Figure 11 shows the most promising correlations. Both atomic and molecular lines are observed to correlate. Two new tight ($|\rho| > 0.9$) correlations between FIR lines are identified: one between [OI] 63.18 μm and CO 144.78 μm, and the other between [OI] 63.18 μm and o-H_2O 78.74 μm. Perhaps statistically less meaningful because of T Tau, we also find correlations between CO 144.78 μm and o-H_2O 63.32 μm, and between OH 79.12+79.18 μm and o-H_2O 78.74 μm. The correlation between [OI] 63.18 μm and o-H_2O 63.18 μm has already been observed in T Tauri stars (Riviere-Marichalar et al. 2012).

6. Discussion

The [OI] 63.18 μm line can arise in the surface of discs depending on disc size and spectral type (Gorti & Hollenbach 2008). It can be produced in photodissociation regions (PDRs; Tielens & Hollenbach 1985), in shocks (Neufeld & Hollenbach 1994), or in the envelopes of Class I sources (Ceccarelli et al. 1996). Nothing precludes all mechanisms from contributing simultaneously. Given that the majority of our objects are Class II (see Sect. 2), whose envelopes are likely already dissipated, we dedicate the following sections to a discussion of the most probable ones, i.e. shocks and discs. Each scenario is considered separately; line fluxes and their line ratios (see Appendix C) are compared with shock and disc model predictions. We stress that in both scenarios a contribution from PDRs is also expected.

6.1. Emission in a shock scenario

Jets, outflows, and winds associated with PMS (pre-main sequence) stars can be traced with forbidden lines, e.g.

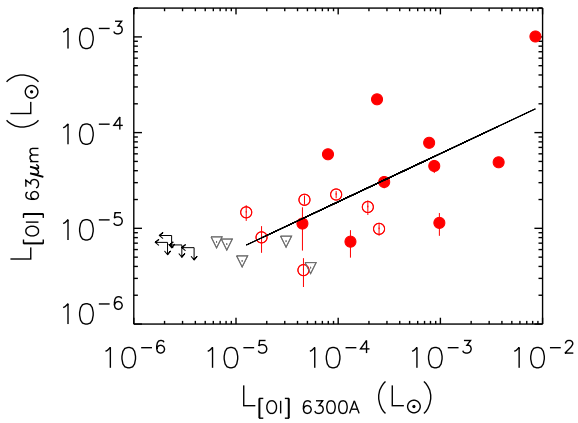

Fig. 12. [OI] 63.18 μm as a function of [OI] 6300 Å line luminosities in solar units. The fit is only for detections and is indicated by the solid line. The red circles represent detections, grey triangles are upper limits in their pointing direction, and black arrows are upper limits in both axes. Filled symbols represent outflow sources.

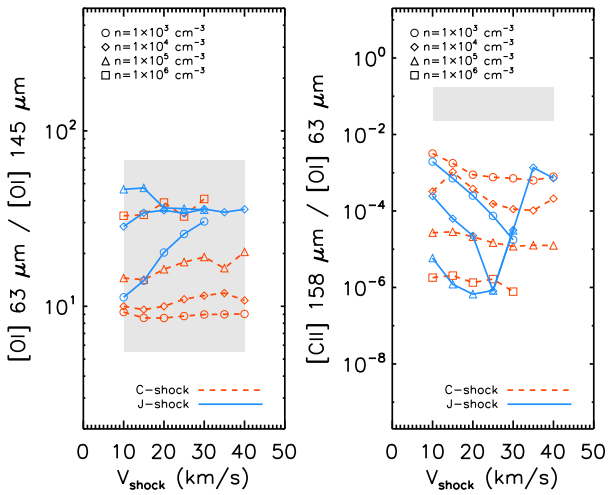

Fig. 13. Observed atomic line ratios compared to C-type (red dashed lines) and J-type (blue lines) shock model predictions from Flower & Pineau des Forêts (2015) for shock velocities (V_{shock}) between 10 and 40 km s^{-1}. The circles, diamonds, triangles, and squares correspond to pre-shock densities (n) of 10^3 cm^{-3}, 10^4 cm^{-3}, 10^5 cm^{-3}, and 10^6 cm^{-3}, respectively. The range of the observed atomic ratios is represented by the shaded region.

[OI] 6300 Å (e.g. Appenzeller & Mundt 1989; Edwards et al. 1993; Hirth et al. 1997). A correlation between these jet/outflow tracers and FIR lines would suggest a similar origin. Figure 12 shows the [OI] 63.18 μm luminosity as a function of the [OI] 6300 Å line luminosity from Hartigan et al. (1995) integrated over the entire profile. The lines correlate ($\rho \sim 0.89$; see Sect. 5.2), pointing to a common origin for the two lines. It is not clear whether the non-outflow sources with relatively bright [OI] emission are associated with fainter unidentified compact outflows located within the central spaxel (9.4″). The observed scatter could be due to the presence of several velocity components. Indeed, the [OI] 6300 Å line profile often shows two velocity components (Hartigan et al. 1995): a high velocity component (HVC) shifted by 50–200 km s^{-1} with respect to the stellar velocity, tracing collimated jets, and a low velocity component (LVC) shifted by 5–20 km s^{-1}, whose origin is possibly due to a photoevaporative wind (Rigliaco et al. 2013; Simon et al. 2016). Unfortunately, the PACS spectral resolution at 63 μm is ~88 km s^{-1}, not high enough to resolve velocity components, but we note that in several cases the wings are broad. Such broadening is observed in the red wing of the [OI] 63.18 μm line profile (see Fig. F.1) of CW Tau, DO Tau, DQ Tau, FS Tau, Haro6-5 B, HV Tau, and RW Aur. Interestingly, the [OI] 6300 Å and [OI] 63.18 μm line profiles of RW Aur do not show the same line shape, but have roughly the same 300 km s^{-1} broadening. This further suggests the presence of several components like in HH 46 (van Kempen et al. 2010) and DK Cha (Riviere-Marichalar et al. 2014).

6.1.1. Atomic line ratios as tracers of the excitation conditions

The line ratios of [OI]63/[OI]145 combined with [CII]158/[OI]63 can be used as diagnostics of the excitation mechanisms (e.g. Nisini et al. 1996; Kaufman et al. 1999). The [OI]63/145 ratios of our sample are between ~10 and 70 with a median of ~23, therefore compatible with ISO observations (Liseau et al. 2006) and the ratios observed in Herbig Ae/Be stars (Meeus et al. 2012; Fedele et al. 2013). There is no statistical difference in terms of [CII]/[OI] line ratios between extended objects (detected in more than one spaxel but not incorrectly pointed) and compact objects (only detected in one spaxel) in our sample. We note that in those sources with extended outflow emission, the ISO and *Herschel* absolute fluxes are not expected to be similar, due to the much larger beam and a lack of background emission subtraction in ISO.

Figure 13 shows the observed atomic line ratios compared to shock model predictions by Flower & Pineau des Forêts (2015). Both C- and J-type shocks can reproduce a [OI]63/[OI]145 line ratio for a wide range of shock parameters (V_{shock} and n). However, such models fail to explain the observed [CII]158/[OI]63 ratios. This is not surprising as [CII] is thought to arise in PDRs. To further disentangle the origin of [OI] and [CII] lines, in Fig. 14 we combined [OI]63/[OI]145 and [CII]158/[OI]63 atomic line ratios and compared them to the PDR models of Kaufman et al. (1999) and the higher velocity ($V_{shock} > 50$ km s^{-1}) J-shock models by Hollenbach & McKee (1989). Figure 14 indicates that the observed ratios are all compatible with PDR models with densities between ~10^3 and 10^6 cm^{-3} and FUV fields $G_0 > 10^2$; only a few cases are compatible with fast J-shocks with low pre-shock densities ($V_{shock} = 50$–130 km s^{-1}, $n \sim 10^3$ cm^{-3}), or both. The sources whose line ratios are compatible with shocks lie in a region in which the models overlap. Thus, it is impossible to discern which phenomenon is responsible for the emission. Similar PDR and shock parameters were obtained by Podio et al. (2012). Although weak [CII] in shocks is predicted by models (Flower & Pineau Des Forêts 2010), the [CII] 157.74 μm line is more likely to originate in PDRs, as studies based on SOFIA/GREAT (Heyminck et al. 2012) observations suggest (e.g. Sandell et al. 2015; Okada et al. 2015).

In the few cases where [CII] 157.74 μm has been spectroscopically resolved with *Herschel*/HIFI, it is clear that the line is not due to a disc, but rather to a remnant envelope or a diffuse cloud (HD 100546, Fedele et al. 2013), or even to PDR emission in the outflow (DG Tau, Podio et al. 2013). PACS observations of Upper Scorpius, have revealed low [CII] fluxes in two T Tauri stars (Mathews et al. 2013). These are early K-type protoplanetary systems without any signature of

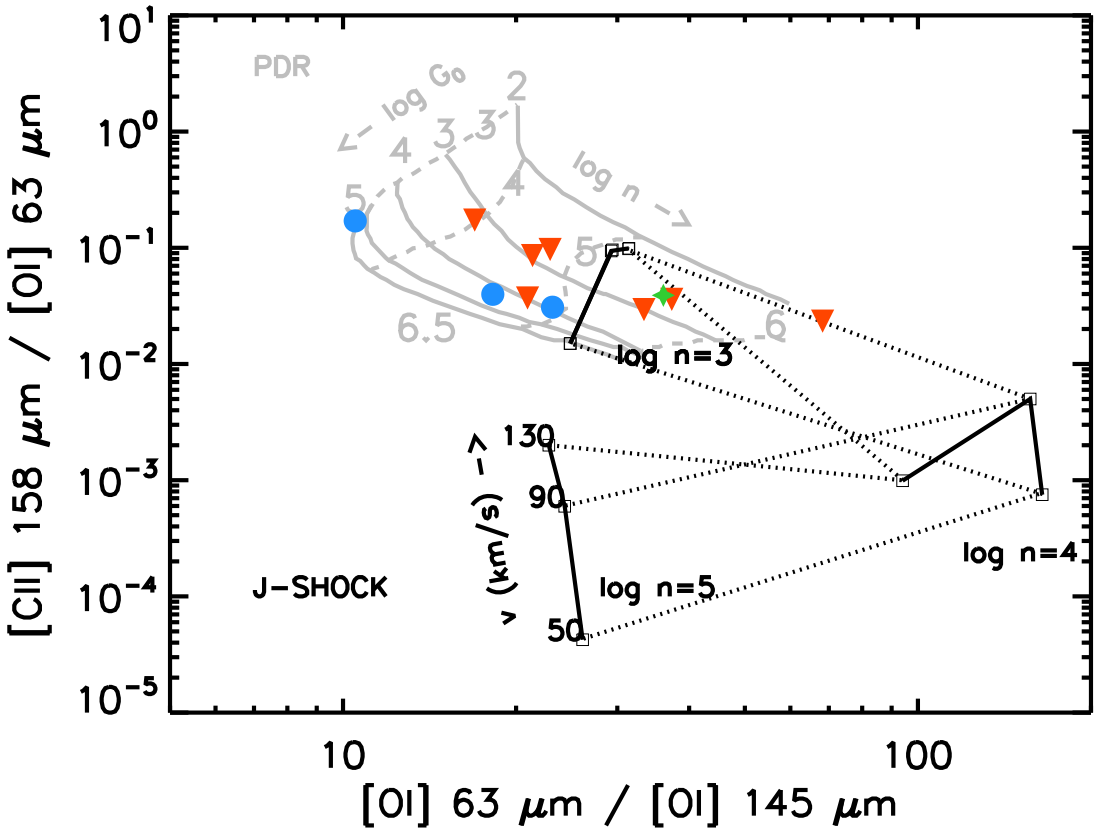

Fig. 14. Observed [OI]63/[OI]145 and [OI]63/[CII]158 line flux ratios plotted as a function of different emitting conditions. The PDR models (grey) are from Kaufman et al. (1999); and J-shock models (black) from Hollenbach & McKee (1989). For the PDR models, the labels indicate the gas density (n) and the intensity of the FUV field (G_0), respectively. For the shock models, the labels denote pre-shock densities (n) and shock speeds ($V_{\rm shock}$). The data is plotted according to their SED class: blue circles are Class I, red triangles are Class II, and green stars are TD.

jet/outflow emission, further suggesting that [CII] 157.74 μm emission is PDR dominated.

6.1.2. Molecular line ratios as tracers of excitation conditions

Figure 15 shows a combination of molecular line ratios compared to C-type and J-type shock models from Flower & Pineau des Forêts (2015). The excitation conditions are, within errors, compatible with both C- and J-type shocks, with pre-shock densities between 10^4 cm^{-3} and 10^6 cm^{-3} and $V_{\rm shock}$ = 15–30 km s^{-1} for most of the sources. The agreement between observations and shock model predictions depends on the specific line ratio (see Karska et al. 2014b) and the evolutionary stage of each source. Similar conditions are found in the few cases where individual sources have been compared to shock models (Lee et al. 2013; Dionatos et al. 2013). However, we must stress that C-type shocks are probably the main driver of the molecular emission (see below).

Non-outflow sources show low J CO and "hot" ($T_{\rm ex}$ > 1000 K) o-H_2O line detections. In addition, outflow sources also show high J CO and "cold" ($T_{\rm ex}$ < 700 K) o-H_2O lines. This indicates that high J CO transitions ($J_{\rm up}$ ≥ 20 in Karska et al. 2014a) are harder to excite in discs (Woitke et al. 2009), whereas shocks can account for such emission (van Kempen et al. 2010; Visser et al. 2012); in addition, the fact that combinations of hot and cold o-H_2O lines are compatible with shock models (upper panels of Fig. 15) with similar parameters suggests that H_2O (and CO) can arise in similar regions.

The OH/H_2O line ratios (see lower right panel of Fig. 15) can only reproduce the excitation conditions of HL Tau, which shows emission from very hot water lines (Kristensen et al. 2016). Karska et al. (2014b) could not reproduce those line ratios for their sample of Class 0/I source in Perseus. The discrepancy between observations and models depends on the H_2O transition that are used because dissociative radiation (Lyman α photons) may have an impact on the composition of the pre-shocked gas (Flower & Pineau des Forêts 2015), hence affecting the abundance of H_2O (Melnick & Kaufman 2015). *Spitzer* mid-IR observations of OH in DG Tau by Carr & Najita (2014) support the idea of hot OH emission induced by dissociation of H_2O by FUV radiation. *Herschel* observations of OH in the range 70–160 μm indicate that the OH emission originates from dissociative shocks in young stellar objects (Class 0/I in Wampfler et al. 2010). Further modelling of the OH radical by Wampfler et al. (2013) with radiative transfer codes of spherical symmetric envelopes could not reproduce the OH line fluxes nor the line widths, strongly suggesting that the OH is coming from shocked gas.

There is evidence pointing to C-type rather than to J-type shocks as the main mechanisms driving the excitation of molecular FIR lines (see Karska et al. 2014b, for a discussion). The [OI]/H_2O line ratios can be used to discern between shock types. We followed the criteria established by Lee et al. (2014). The division between J- and irradiated C-type shocks occurs when [OI]/H_2O ~ 100, indicative of water photodissociation. The division between irradiated C-type and normal C-type occurs when [OI]/H_2O ~ 1. Table 3 lists the [OI]/H_2O of our sample. The

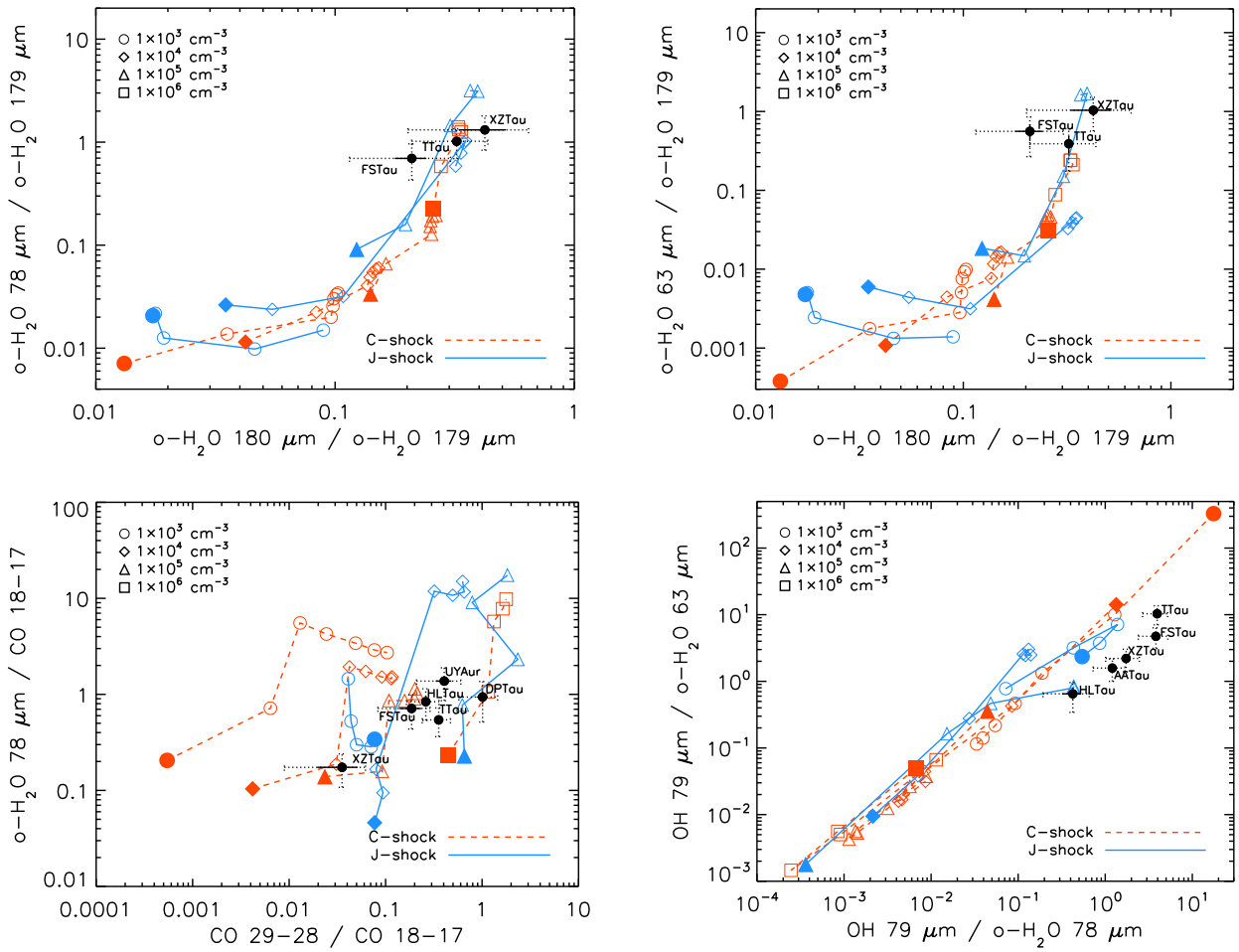

Fig. 15. Observed molecular line ratios compared with C-type (red dashed lines) and J-type (blue lines) model predictions from Flower & Pineau des Forêts (2015). The circles, diamonds, triangles, and squares correspond to pre-shock densities of 10^3 cm^{-3}, 10^4 cm^{-3}, 10^5 cm^{-3}, and 10^6 cm^{-3}, respectively, with shock velocities ($V_{\rm shock}$) from 10 km s^{-1} to 40 km s^{-1} (C-type) or from 10 km s^{-1} to 30 km s^{-1} (J-type). Filled symbols indicate the position of the lowest velocity ($V_{\rm shock}$=10 km s^{-1}). Black filled circles represent detections and arrows are upper limits. Solid error bars are the intrinsic errors of the line fluxes and dotted error bars are obtained by adding a 30% error due to the PACS flux calibration.

ratios of the outflow sources are compatible with irradiated C-shocks; and only in XZ Tau ([OI]/H_2O > 100) a fast J-type shock may also contribute to the emission. The line ratios of the non-outflow sources BP Tau, GI/GK Tau, and IQ Tau are low (1 < [OI]/H_2O < 2). It is unclear whether such low ratios are compatible with weak outflow activity within the size of the PACS central spaxel (9.4″) or a disc.

To further test the shock scenario we follow the Flower & Pineau des Forêts (2015) models to estimate the size (D) of the emitting areas (see Table 4) necessary to reproduce the observed molecular line fluxes. If the emission is indeed associated with shocked gas, the emitting areas have to be compatible with the observed scales (10 arcsec level) of molecular gas in T Tauri stars. The OH areas are computed assuming that the same physical conditions ($V_{\rm shock}$ and n) as for HL Tau holds for all detected objects. Details of the derivation are in Appendix E. We find that the emitting areas range from tens to hundreds of au, consistent with molecular emission being compact and unresolved with PACS at the distance of Taurus. The CO emitting areas are larger than those of H_2O, found to be between tens of au and a few hundred. In particular, the size of the H_2O emitting area for T Tau is comparable with previous estimates (Spinoglio et al. 2000; Podio et al. 2012), and compatible with those obtained by Mottram et al. (2015) for Class 0/I sources.

Concerning the spatial extent of H_2O compared to [OI] along the outflow, in the maps presented in Nisini et al. (2015) the two species (o-H_2O 179.53 μm and [OI] 63.18 μm) show a similar extent. However, this depends on the H_2O line considered because various transitions require different physical conditions for excitation. Even in the case of jet/outflow emission, the water lines can originate in much denser – and probably more confined – regions compared to [OI].

6.2. Emission in a disc scenario

6.2.1. Disc contribution to [OI]

We now compare the observed fluxes with dust tracers, i.e. infrared continuum, to try to determine the contribution of the disc to the line emission.

Figure 16 represents the flux of the [OI] 63.18 μm line as a function of *Spitzer*/IRAC 3.6, 8.0 μm, *Spitzer*/MIPS 24 μm, and PACS 70 μm (Rebull et al. 2010; Luhman et al. 2010; Howard et al. 2013). The outflow sources are clearly brighter than non-outflow ones. While there is no obvious trend with 3.6 μm and the scatter is large at 8.0 μm, there is a clear trend at 24 and 70 μm. Longer continuum wavelengths are associated with colder dust, probing deeper in and further out disc regions.

Table 3. [OI]/o-H_2O line ratios.

Target (1)	63/63 (2)	63/78 (3)	63/179 (4)	63/180 (5)
AA Tau	1.78	1.35	–	–
BP Tau	1.25	–	–	–
DL Tau	2.33	–	–	–
DP Tau	–	11.16	–	–
FS Tau	29.34	23.63	16.43	78.53
GG Tau	–	14.47	–	–
GI/GK Tau	1.84	–	–	–
Haro6-5B	2.87	3.66	–	–
Haro6-13	–	10.42	–	–
HL Tau	8.86	5.79	–	–
HN Tau	9.19	–	–	–
IQ Tau	1.60	–	–	–
IRAS04385+2550	–	8.22	–	–
RW Aur	–	–	9.24	–
RY Tau	4.80	7.27	–	–
T Tau	74.12	28.34	28.88	89.66
UY Aur	–	10.47	24.19	–
XZ Tau	55.33	43.56	57.30	135.59

Notes. All the targets listed in Col. (1) have [OI] 63.18 μm detected. Columns (2) to (5) show the line ratios between the [OI] line at 63.18 μm and o-H_2O lines at 63.32, 78.74, 179.53, and 180.49 μm, respectively; otherwise is indicated by "–".

Table 4. Diameter (in au) of the emitting area for H_2O, CO, and OH estimated from *C*- and *J*-type shock models.

Source	$D(H_2O)$	D(CO)	D(OH)
AA Tau	–	–	102–109
DP Tau	–	56–122	–
FS Tau A	33–99	184–395	261–277
HL Tau	–	339–821	174–183
T Tau	160–364	307–610	1613–1701
UY Aur	–	53–115	212–225
XZ Tau	33–97	225–730	170–181

At longer wavelengths it is more likely that continuum and FIR line emission both come from the same radial zone.

The distribution of Taurus sources in the [OI]–infrared diagrams is connected with the evolutionary status of the sources and the presence of outflows. The different behaviour of outflow/non-outflow sources in such diagrams has already been pointed out by Howard et al. (2013). The correlation between the line flux and the dust emission for non-outflow sources suggests that both arise in the disc. The contribution of the disc to the gas emission in the outflow sources can be estimated assuming that the [OI]–70 micron correlation for non-outflow sources holds for all discs. In the case that outflow and non-outflow sources show similar trends with continuum emission, this test cannot distinguish clearly between the two origins or whether outflow emission does not have a relevant effect. A linear fit to our data for such correlation is given by

$$\log_{10}(F_{[\mathrm{OI}]63\ \mu\mathrm{m}}) = -16.82 + 0.40 \times \log_{10}(F_{70\ \mu\mathrm{m}}), \quad (1)$$

where $F_{[\mathrm{OI}]63\ \mu\mathrm{m}}$ is the [OI] 63.18 μm line flux in W m^{-2} and $F_{70\ \mu\mathrm{m}}$ is the continuum flux at 70 μm in Jy. Table 5 shows the disc contribution in terms of the SED Classes. The relative contribution from the disc increases as the system evolves. In Class I sources the disc contributes ~20% and it keeps increasing until outflow activity dissipates. This is clear when comparing Class II sources with and without outflows (38% compared to 100%). This is in agreement with Podio et al. (2012) who obtained a disc contribution between 3% and 15% for Class I and Class II sources with outflows and showing [OI] 63.18 μm extended emission. In the case of T Tau the disc contribution (<1%) is negligible.

Table 5. Ranges and mean (median) values of disc contribution in percentage to the [OI] 63.18 μm line flux for different SED classes.

SED Class	Range	Mean (median)	*N* sources
Class I	1–51%	19% (18%)	4
ClassII+Jet	3–100%	38% (24%)	11
TD+Jet	43%	43% (43%)	1
ClassII	65–100%	92% (99%)	7
TD	100%	100% (100%)	2

Table 6. Comparison of the slopes (with errors) between the strength of the water lines and OI observed, and the predictions by Aresu et al. (2012) for two different models.

λ (μm)	Transition	Observed	UV model	UV+X-ray model
63.32	8_{18}–7_{07}	0.41(0.06)	0.96(0.07)	0.73(0.12)
78.74	4_{23}–3_{12}	0.65(0.10)	–	–
179.53	2_{12}–1_{01}	0.81(0.18)	0.02(0.01)	0.32(0.07)

6.2.2. Disc contribution to H_2O

We showed (see Sect. 5.2) that the o-H_2O 63.32, 78.74 and 179.53 μm line luminosities correlate with [OI] 63.18 μm ($\rho > 0.9$). The slopes of the fit become steeper for lower excitation energies of the water transition (Table 6). The hydrostatic equilibrium models by Aresu et al. (2012) showed that the amount UV and X-ray radiation in a disc influences the line luminosities, and predicted the slopes between the different line luminosities. Their models do not match our observed water line luminosities and fail to reproduce the slopes we observe. The predictions from the fully parametrized DENT disc grid do reproduce the observed H_2O/[OI] and CO/[OI] ratios, but fail to explain the high H_2O and CO fluxes (Podio et al. 2012), suggesting that an additional component and/or different gas-to-dust ratios are needed to account for these high fluxes. In order to account for these discrepancies, higher disc masses and/or low dust-to-gas ratios, high FUV fluxes, or discs heated by X-rays (Aresu et al. 2011, 2012) are needed. Indeed, Podio et al. (2013) showed that a model of DG Tau with a massive gaseous disc associated with strong UV and X-ray radiation reproduces the H_2O lines well. Other options include a more complicated inner disc structure, such as a puffed up inner rim (Aresu et al. 2011, 2012), gap, or hole.

6.3. Jet or disc?

From our analysis described above, a jet/outflow origin is favoured for the strong FIR lines because of (1) the observed extended emission in outflow sources (see maps in e.g. Nisini et al. 2010; Podio et al. 2012; Nisini et al. 2015); (2) the detections predominantly in outflow sources and the correlations between emission lines; and (3) the compatibility of line ratios with shock models especially for Class I sources for which the disc

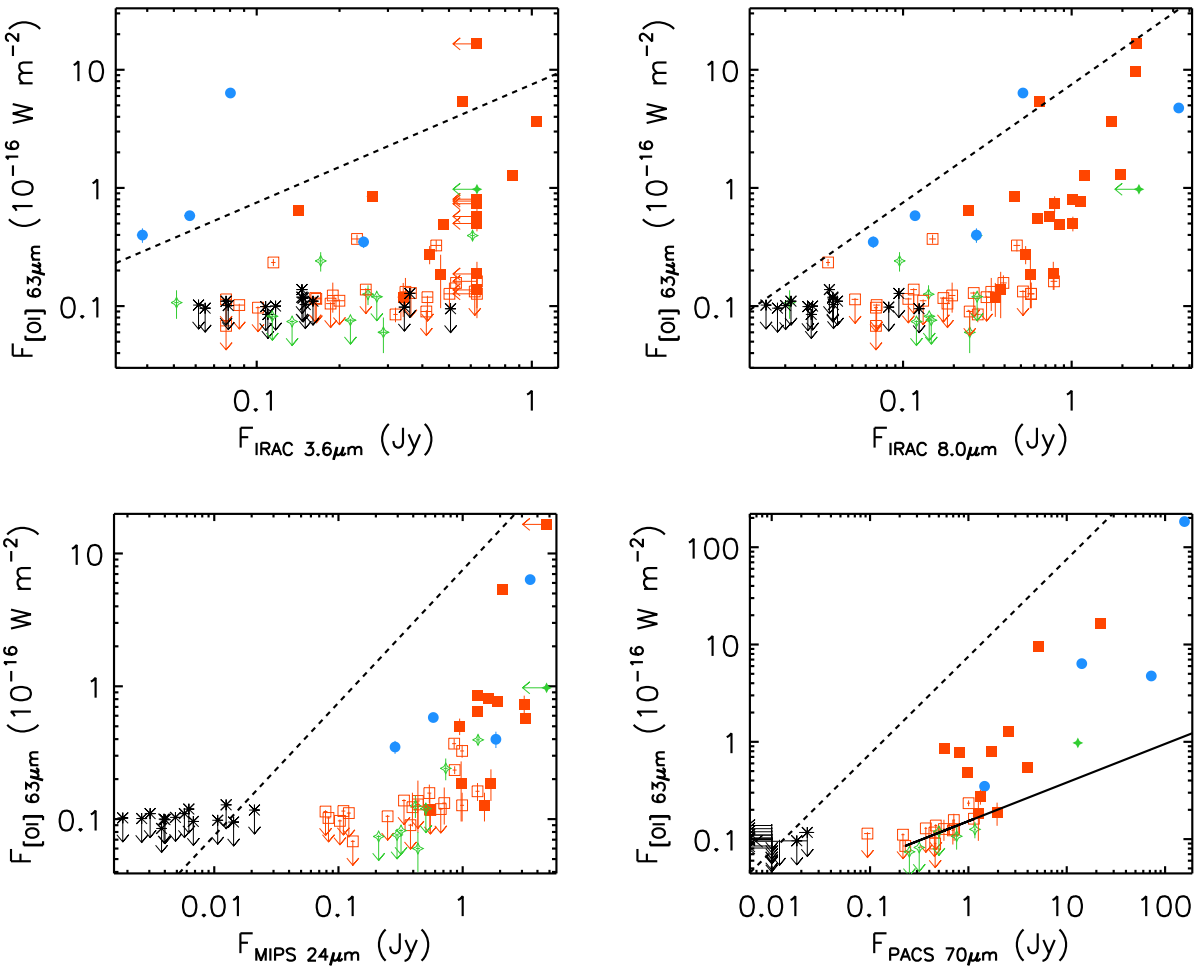

Fig. 16. [OI] 63.18 μm flux versus: IRAC 3.6 μm (*top left*); IRAC 8.0 μm (*top right*); MIPS 24 μm (*bottom left*); and PACS 70 μm (*bottom right*) continuum fluxes. Class I, Class II, Class III, and transition discs (TD) are represented by circles (blue), squares (red), asterisks (black), and stars (green), respectively. Filled symbols corresponds to outflow sources. Arrows indicate upper limits. The dashed lines are 1:1 relations and the solid line is a fit to disc sources as explained in the text.

contribution is estimated to be smaller than 20%. Nonetheless, we note the following: (1) several detections of [OI] and o-H_2O at 63 μm in non-outflow sources; (2) correlations between the line fluxes and continuum for 24 and 70 μm, which point to a disc origin; (3) compact molecular emission within the PACS beam also observed in Class I sources, which have (small) outflows; and (4) gas line ratios reproduced satisfactorily by the disc models (e.g. Kamp et al. 2011; Aresu et al. 2012). Therefore, the excitation mechanism in discs should not be the main problem. Different dust-to-gas ratios, larger scale heights, or inner gaps would make the disc likely hotter than a normal continuous disc model, but other agents may only increase the emitting surface area. This particular issue cannot be fully understood without spectroscopically and spatially resolved observations, so that the location and dynamics of the emitting gas can be pin-pointed; however, for FIR observations this is hard to obtain. A promising alternative to this problem could be to use lines which are likely co-spatial with some of the FIR lines, such as ro-vibrational lines of CO (see e.g. Banzatti & Pontoppidan 2015). This way, one could determine whether the lines are purely associated with a Keplerian disc or coming from shocks via jets and/or winds. Within a disc, gas kinematics derived from resolved line profiles may help disentangle various regions, especially at shorter wavelengths where the spatial resolution is higher.

7. Summary and conclusions

We provide a catalogue of line fluxes in the FIR (63–190 μm) for T Tauri stars located in Taurus, surveyed with *Herschel*/PACS as part of the GASPS project. The species observed include [OI], [CII], CO, H_2O, and OH. The origin of the atomic and molecular emission is investigated by comparing line fluxes and line ratios to shock and disc models. The main conclusions are as follows:

- Outflow sources exhibit brighter atomic and molecular emission lines and higher detection rates than non-outflow sources. In agreement with previous studies, atomic and molecular FIR line emission in T Tauri systems is observed to decrease with evolutionary stage.
- The [OI] line emission is brighter and more often detected in systems with signs of jet/outflows and in early phases of stellar evolution (Classes I and II), suggesting a dominant contribution from shocks in young outflow systems. In these systems the emission is spatially extended (10 arcsec level). Slow (V_{shock} = 10–50 km s^{-1}) J- and C-type shocks with densities between n = 10^3 and 10^6 cm^{-3}) can reproduce the observed [OI]63/[OI]145 ratios. These models do not reproduce the [CII]158/[OI]63 line ratios well. Fast (V_{shock} = 50–130 km s^{-1}) J-shocks at low densities (n = 10^3 cm^{-3}) and/or

PDR models ($n > 10^3$ cm^{-3}, $G_0 > 10^2$) can reproduce the combined [OI]63/[OI]145 and [CII]158/[OI]63 line ratios.
- The main contribution to the [CII] 157.74 μm line most probably come from PDR emission from the disc and its surroundings. A (small) contribution from shocks is also expected, as detections only in outflow sources and shock models suggest. The precise origin of the [CII] line has to be better constrained with spatially and spectroscopically resolved observations.
- The observed correlations support the interpretation of jet/outflows (when present) as the dominant contributor to the FIR line emission, and points to a common excitation mechanism, i.e. shocks. The broad wings of the [OI] 63.18 μm line and its correlation with [OI] 6300 Å suggest the presence of several velocity components, i.e. a jet origin for the HVC and a combination of disc, envelope, and wind for the LVC.
- Molecular line emission (H_2O, CO, and OH) is also mainly detected in outflow systems. Slow (V_{shock} = 15–30 km s^{-1}) C-type shocks with densities between $n = 10^4$ and 10^6 cm^{-3} can account for these fluxes; with emitting areas ranging from tens to hundreds of au. The OH/H_2O line ratios are typically overestimated in J-type shocks.
- The correlations with photometric bands (24 and 70 μm) indicate that the contribution from the disc to the [OI] 63.18 μm line flux may be up to ~50% for the jet/outflow sources, strongly depending on the evolutionary status of the source. When the jet/outflow activity decreases, the disc contribution relative to the line fluxes increases significantly (>65% in Class II sources).
- Although there are clear indications that the emission is dominated by the outflow, massive discs and/or low dust-to-gas ratios may also explain the observed high molecular line fluxes.

The low spectral and spatial resolution from PACS are not sufficient to unambiguously determine what fraction of the line emission comes from the disc, outflow, or the surrounding envelope. Spatially and/or velocity resolved observations are needed to pin-point the origin of the emission lines. In this regard, the instruments on board SOFIA may have the potential to resolve the brightest lines. Models which include both a disc and a jet/outflow and their interaction are needed to accurately interpret the multiwavelength observations of young T Tauri stars.

Acknowledgements. M. Alonso-Martinez, C. Eiroa, and G. Meeus are partially supported by AYA2011–26202 and AYA2014–55840–P. G.M. is supported by RyC–2011–07920. P.R.M. acknowledges funding from the ESA Research Fellowship Programme. I.K. acknowledges funding from the European Union Seventh Framework Programme FP7-2011 under grant agreement No. 284405. L.P. has received funding from the European Union Seventh Framework Programme (FP7/2007–2013) under grant agreement No. 267251. We would also like to thank the anonymous referee for the constructive comments which certainly helped to substantially improve the quality of the paper. This research has made use of the SIMBAD database, operated at CDS, Strasbourg, France.

References

Agra-Amboage, V., Dougados, C., Cabrit, S., Garcia, P. J. V., & Ferruit, P. 2009, A&A, 493, 1029
Agra-Amboage, V., Dougados, C., Cabrit, S., & Reunanen, J. 2011, A&A, 532, A59
Andrews, S. M., & Williams, J. P. 2005, ApJ, 631, 1134
Appenzeller, I., & Mundt, R. 1989, A&ARv, 1, 291
Aresu, G., Kamp, I., Meijerink, R., et al. 2011, A&A, 526, A163
Aresu, G., Meijerink, R., Kamp, I., et al. 2012, A&A, 547, A69
Bally, J., Reipurth, B., & Davis, C. J. 2007, in Protostars and Planets V, eds. B. Reipurth, D. Jewitt & K. Keil (Tucson: University of Arizona Press), 215
Banzatti, A., & Pontoppidan, K. M. 2015, ApJ, 809, 167
Beckwith, S. V. W., Sargent, A. I., Chini, R. S., & Guesten, R. 1990, AJ, 99, 924
Burgasser, A. J., Kirkpatrick, J. D., Reid, I. N., et al. 2003, ApJ, 586, 512
Cabrit, S., Ferreira, J., & Dougados, C. 2011, in Jets at all scales, IAU Symp. 275, eds. G. E. Romero, R. A. Sunyaev, & T. Belloni, 374
Calvet, N., Muzerolle, J., Briceño, C., et al. 2004, AJ, 128, 1294
Cardelli, J. A., Clayton, G. C., & Mathis, J. S. 1989, ApJ, 345, 245
Carr, J. S., & Najita, J. R. 2014, ApJ, 788, 66
Ceccarelli, C., Hollenbach, D. J., & Tielens, A. G. G. M. 1996, ApJ, 471, 400
Daemgen, S., Bonavita, M., Jayawardhana, R., Lafrenière, D., & Janson, M. 2015, ApJ, 799, 155
Dent, W. R. F., Thi, W. F., Kamp, I., et al. 2013, PASP, 125, 477
Dionatos, O., Jørgensen, J. K., Green, J. D., et al. 2013, A&A, 558, A88
Dutrey, A., Semenov, D., Chapillon, E., et al. 2014, Protostars and Planets VI (Tucson: University of Arizona Press), 317
Edwards, S., Ray, T., & Mundt, R. 1993, in Protostars and Planets III, eds. E. H. Levy, & J. I. Lunine (Tucson: University of Arizona Press), 567
Eislöffel, J., & Mundt, R. 1998, AJ, 115, 1554
Fedele, D., Bruderer, S., van Dishoeck, E. F., et al. 2013, A&A, 559, A77
Fedele, D., Bruderer, S., van den Ancker, M. E., & Pascucci, I. 2015, ApJ, 800, 23
Flower, D. R., & Pineau Des Forêts, G. 2010, MNRAS, 406, 1745
Flower, D. R., & Pineau des Forêts, G. 2015, A&A, 578, A63
France, K., Schindhelm, E., Bergin, E. A., Roueff, E., & Abgrall, H. 2014, ApJ, 784, 127
Frank, A., Ray, T. P., Cabrit, S., et al. 2014, Protostars and Planets VI (Tucson: University of Arizona Press), 451
Ghez, A. M., Neugebauer, G., & Matthews, K. 1993, AJ, 106, 2005
Goicoechea, J. R., Joblin, C., Contursi, A., et al. 2011, A&A, 530, L16
Gorti, U., & Hollenbach, D. 2008, ApJ, 683, 287
Güdel, M., Briggs, K., Arzner, K., et al. 2007a, in Star-Disk Interaction in Young Stars, IAU Symp., 243, eds. J. Bouvier, & I. Appenzeller, 155
Güdel, M., Briggs, K. R., Arzner, K., et al. 2007b, A&A, 468, 353
Gullbring, E., Hartmann, L., Briceno, C., & Calvet, N. 1998, ApJ, 492, 323
Hamann, F., Simon, M., & Ridgway, S. T. 1988, ApJ, 326, 859
Hartigan, P., Edwards, S., & Ghandour, L. 1995, ApJ, 452, 736
Hartmann, L. 2008, Physica Scripta Volume T, 130, 014012
Herczeg, G. J., & Hillenbrand, L. A. 2014, ApJ, 786, 97
Herczeg, G. J., Karska, A., Bruderer, S., et al. 2012, A&A, 540, A84
Heyminck, S., Graf, U. U., Güsten, R., et al. 2012, A&A, 542, L1
Hirth, G. A., Mundt, R., & Solf, J. 1997, A&AS, 126, 437
Hollenbach, D., & McKee, C. F. 1989, ApJ, 342, 306
Howard, C. D., Sandell, G., Vacca, W. D., et al. 2013, ApJ, 776, 21
Ingleby, L., Calvet, N., Herczeg, G., et al. 2013, ApJ, 767, 112
Jonkheid, B., Faas, F. G. A., van Zadelhoff, G.-J., & van Dishoeck, E. F. 2004, A&A, 428, 511
Kamp, I., & Dullemond, C. P. 2004, ApJ, 615, 991
Kamp, I., Woitke, P., Pinte, C., et al. 2011, A&A, 532, A85
Kamp, I., Thi, W.-F., Meeus, G., et al. 2013, A&A, 559, A24
Karska, A., Herczeg, G. J., van Dishoeck, E. F., et al. 2013, A&A, 552, A141
Karska, A., Herpin, F., Bruderer, S., et al. 2014a, A&A, 562, A45
Karska, A., Kristensen, L. E., van Dishoeck, E. F., et al. 2014b, A&A, 572, A9
Kaufman, M. J., Wolfire, M. G., Hollenbach, D. J., & Luhman, M. L. 1999, ApJ, 527, 795
Keane, J. T., Pascucci, I., Espaillat, C., et al. 2014, ApJ, 787, 153
Kenyon, S. J., & Hartmann, L. 1995, ApJS, 101, 117
Kristensen, L. E., Brown, J. M., Wilner, D., & Salyk, C. 2016, ApJ, 822, L20
Lada, C. J. 1987, in Star Forming Regions, eds. M. Peimbert, & J. Jugaku, IAU Symp., 115, 1
Lee, J., Lee, J.-E., Lee, S., et al. 2013, ApJS, 209, 4
Lee, J.-E., Lee, J., Lee, S., Evans, II, N. J., & Green, J. D. 2014, ApJS, 214, 21
Liseau, R., Justtanont, K., & Tielens, A. G. G. M. 2006, A&A, 446, 561
Luhman, K. L., Allen, P. R., Espaillat, C., Hartmann, L., & Calvet, N. 2010, ApJS, 186, 111
Lynch, C., Mutel, R. L., Güdel, M., et al. 2013, ApJ, 766, 53
Manoj, P., Green, J. D., Megeath, S. T., et al. 2016, ApJ, 831, 69
Marseille, M. G., van der Tak, F. F. S., Herpin, F., & Jacq, T. 2010, A&A, 522, A40
Mathews, G. S., Dent, W. R. F., Williams, J. P., et al. 2010, A&A, 518, L127
Mathews, G. S., Pinte, C., Duchêne, G., Williams, J. P., & Ménard, F. 2013, A&A, 558, A66
McGroarty, F., Ray, T. P., & Bally, J. 2004, Baltic Astron., 13, 528
Meeus, G., Montesinos, B., Mendigutía, I., et al. 2012, A&A, 544, A78
Melnick, G. J., & Kaufman, M. J. 2015, ApJ, 806, 227
Mottram, J. C., Kristensen, L. E., van Dishoeck, E. F., et al. 2015, A&A, 574, C3
Najita, J., Carr, J. S., & Mathieu, R. D. 2003, ApJ, 589, 931

Najita, J. R., Strom, S. E., & Muzerolle, J. 2007, MNRAS, 378, 369
Neufeld, D. A., & Hollenbach, D. J. 1994, ApJ, 428, 170
Nisini, B., Lorenzetti, D., Cohen, M., et al. 1996, A&A, 315, L321
Nisini, B., Giannini, T., & Lorenzetti, D. 2002, ApJ, 574, 246
Nisini, B., Benedettini, M., Codella, C., et al. 2010, A&A, 518, L120
Nisini, B., Santangelo, G., Giannini, T., et al. 2015, ApJ, 801, 121
Öberg, K. I., Qi, C., Fogel, J. K. J., et al. 2011, ApJ, 734, 98
Okada, Y., Requena-Torres, M. A., Güsten, R., et al. 2015, A&A, 580, A54
Ott, S. 2013, in ASP Conf. Ser. 475, ed. D. N. Friedel, 197
Palla, F., & Stahler, S. W. 2002, ApJ, 581, 1194
Pascucci, I., Gorti, U., Hollenbach, D., et al. 2006, ApJ, 651, 1177
Piétu, V., Dutrey, A., & Guilloteau, S. 2007, A&A, 467, 163
Pilbratt, G. L., Riedinger, J. R., Passvogel, T., et al. 2010, A&A, 518, L1
Pinte, C., Woitke, P., Ménard, F., et al. 2010, A&A, 518, L126
Podio, L., Kamp, I., Flower, D., et al. 2012, A&A, 545, A44
Podio, L., Kamp, I., Codella, C., et al. 2013, ApJ, 766, L5
Poglitsch, A., Waelkens, C., Geis, N., et al. 2010, A&A, 518, L2
Rebull, L. M., Padgett, D. L., McCabe, C.-E., et al. 2010, ApJS, 186, 259
Reipurth, B., & Bally, J. 2001, ARA&A, 39, 403
Rigliaco, E., Pascucci, I., Gorti, U., Edwards, S., & Hollenbach, D. 2013, ApJ, 772, 60
Riviere-Marichalar, P., Ménard, F., Thi, W. F., et al. 2012, A&A, 538, L3
Riviere-Marichalar, P., Pinte, C., Barrado, D., et al. 2013, A&A, 555, A67
Riviere-Marichalar, P., Barrado, D., Montesinos, B., et al. 2014, A&A, 565, A68
Riviere-Marichalar, P., Bayo, A., Kamp, I., et al. 2015, A&A, 575, A19
Riviere-Marichalar, P., Merín, B., Kamp, I., Eiroa, C., & Montesinos, B. 2016, A&A, 594, A59
Robrade, J., Schmitt, J. H. M. M., & Hempelmann, A. 2007, Mem. Soc. Astron. Italiana, 78, 311
Sandell, G., Mookerjea, B., Güsten, R., et al. 2015, A&A, 578, A41
Schneider, P. C., Eislöffel, J., Güdel, M., et al. 2013, A&A, 557, A110
Semenov, D. A. 2011, in The Molecular Universe, IAU Symp., 280, eds. J. Cernicharo, & R. Bachiller, 114
Simon, M. N., Pascucci, I., Edwards, S., et al. 2016, ApJ, 831, 169
Spinoglio, L., Giannini, T., Nisini, B., et al. 2000, A&A, 353, 1055
St-Onge, G., & Bastien, P. 2008, ApJ, 674, 1032
Strom, K. M., Strom, S. E., Edwards, S., Cabrit, S., & Skrutskie, M. F. 1989, AJ, 97, 1451
Thi, W.-F., Ménard, F., Meeus, G., et al. 2011, A&A, 530, L2
Tielens, A. G. G. M., & Hollenbach, D. 1985, ApJ, 291, 747
Tilling, I., Woitke, P., Meeus, G., et al. 2012, A&A, 538, A20
van Dishoeck, E. F., Herbst, E., & Neufeld, D. A. 2013, Chem. Rev., 113, 9043
van Kempen, T. A., Kristensen, L. E., Herczeg, G. J., et al. 2010, A&A, 518, L121
Visser, R., Kristensen, L. E., Bruderer, S., et al. 2012, A&A, 537, A55
Wampfler, S. F., Herczeg, G. J., Bruderer, S., et al. 2010, A&A, 521, L36
Wampfler, S. F., Bruderer, S., Karska, A., et al. 2013, A&A, 552, A56
White, R. J., & Ghez, A. M. 2001, ApJ, 556, 265
Williams, J. P., & Cieza, L. A. 2011, ARA&A, 49, 67
Woitke, P., Kamp, I., & Thi, W.-F. 2009, A&A, 501, 383
Woitke, P., Pinte, C., Tilling, I., et al. 2010, MNRAS, 405, L26

Appendix A: Stellar parameters

In Table A.1 we list the literature properties of the sample including SED classes, spectral types, effective temperatures, mass accretion rates, stellar luminosities, X-ray luminosities, accretion luminosities, ages, disc masses, and separation if the sources are multiple systems. The targets are split into outflows and non-outflows depending on their signs of jet/outflow activity as explained in the text (see Sect. 2.1).

Table A.1. Sample properties.

[1]	[2]	[3]	[4]	[5]	[6]	[7]	[8]	[9]	[10]	[11]
Target	SED class	SpT[a]	T^a	$\dot{M}^d_{\rm acc}$	L^c_*	$L^e_{\rm X}$	$L^d_{\rm acc}$	Age[c]	$M^f_{\rm disc}$	Sep. (pair)[g]
[–]	[–]	[–]	[K]	[$10^{-8}\,M_\odot\,{\rm yr}^{-1}$]	[$L_\odot$]	[$L_\odot$]	[$L_\odot$]	[Myr]	[$M_\odot$]	[arcsec]
Outflows										
AA Tau	II	M0.6	3770	2.51	0.74	1.240	0.21	2.7	0.01	...
CW Tau	II	K3	4470	5.27	1.35	2.844	1.01	5.8	0.002	...
DF Tau	II	M2.7	3450	10.05	1.60	...	0.22	0.1	0.0004	0.09 (A–B)
DG Tau	II	K7	4020	25.25	0.90	...	1.26	0.6	0.02	...
DG Tau B	I	M?[b]	<4000	...	...	...	...	...	...	...
DL Tau	II	K5.5	4190	2.48	0.70	...	0.24	2.9	0.09	...
DO Tau	II	M0.3	3830	3.12	1.20	...	0.17	0.6	0.007	...
DP Tau	II	M0.8	3730	0.04	0.41	...	0.01	2.6	<0.0005	...
DQ Tau	II	M0.6	3770	0.59	...	...	0.03	...	0.02	...
FS Tau	II/Flat	M2.4	3510	...	0.32	3.224	...	2.8	0.002	0.23 (A–B)
GG Tau	II	K7.5(A)+M5.8(B)	3930(A)+2890(B)	7.95	0.84(A)+0.71(B)	...	0.41	2.3(A)+1.5(B)	0.2	0.25 (Aa–Ab)
Haro 6–5 B	I	M4	3340[c]	...	0.02	17.551	...	...	...	0.23 (A–B)
Haro 6–13	II	M1.6(E)+K5.5(W)	3670(E)+4190(W)	...	1.30	0.799	...	...	0.01	...
HL Tau	I	K3	4470	0.35	6.60	3.838	0.05	0.1	...	...
HN Tau	II	K3(A)+M4.8(B)	4470(A)+3050(B)	0.49	0.70	...	0.11	22.0	0.0008	3.11 (A–B)
HV Tau	I?	M4.1	3120	...	1.23	...	...	0.3	0.002	3.98 (A–C)
IRAS 04158+2805	I	M3	3470[c]	...	0.41	0.882	...	0.9	...	...
IRAS 04358+2550	II	M0	3850[c]	...	0.36	0.401	...	...	...	...
RW Aur	II	K0(A)+K6.5(B)	5110(A)+4160(B)	...	3.20	...	...	2.8	0.004	1.42 (A–B)
RY Tau	T?	G0	5930	78.18	7.60	5.520	10.21	1.8	0.02	...
SU Aur	II	G4	5560	18.03	12.90	9.464	3.17	2.6	0.0009	...
T Tau	II/I	K0	5250[c]	23.62	15.50	8.048	3.89	1.2	0.008	0.70 (A–B)
UY Aur	II	K7	4020	6.74	3.10	...	0.43	0.8	0.002	0.88 (A–B)
UZ Tau	II	M1.9+M3.1	3560(A)+3410(B)	0.45	1.60(A)+0.52(B)	0.890	0.02	0.2(A)+0.6(B)	0.02	3.54 (A–Ba)
V773 Tau	II	K4	4460	11.95	2.31	9.488	1.03	4.1	0.0005	0.06 (A–B)
XZ Tau	II	M3.2	3370	0.71	3.90	0.962	0.02	0.6	...	0.30 (A–B)
Non-outflows										
BP Tau	II	M0.5	3510	2.80	0.96	1.365	0.22	1.8	0.02	...
CIDA 2	III	M5.5	3200[c]	...	0.29	0.178	...	0.5	<0.0007	...
CI Tau	II	K5.5	4190	12.35	0.87	0.195	2.53	2.1	0.03	...
Coku Tau/4	II	M1.1	3690	...	0.39	...	...	3.0	0.0005	...
CX Tau	T	M2.5	3580	0.04	0.41	...	0.002	1.3	0.001	...
CY Tau	II	M2.3	3515	0.18	0.47	1.94	0.01	1.8	0.006	...
DE Tau	II	M2.3	3515	1.32	0.81	...	0.06	0.4	0.005	...

Notes. [1] Sample targets; [2] SED Class; [3] spectral type; [4] temperature; [5] accretion rate; [6] stellar luminosities; [7] X-ray luminosities; [8] accretion luminosities; [9] stellar age; [10] disc masses; [11] Separation in arcsec and components. The mass accretion rates were derived from the U band excess as follows: first the U band photometry from Kenyon & Hartmann (1995) was derredened using the Cardelli et al. (1989) extinction curve. Then the U band excess was derived by subtracting the photospheric contribution, and converted to accretion luminosity according to the empirical relation $\log(L_{\rm acc}/L_\odot) = 1.09 \times \log(L_U/L_\odot) + 0.98$ in Gullbring et al. (1998). The mass accretion rates were finally obtained using the relation $M_{\rm acc} = \frac{L_{\rm acc} R_\star}{GM_\star(1-R_\star/R_{\rm in})}$, following the assumptions in Gullbring et al. (1998).

References. [a] Herczeg & Hillenbrand (2014), [b] see Howard et al. (2013) for a discussion, [c] Palla & Stahler (2002), [d] $\dot{M}_{\rm acc}$ and $L_{\rm acc}$ as explained above, [e] Güdel et al. (2007b), [f] Andrews & Williams (2005), [g] White & Ghez (2001).

Table A.1. continued.

[1]	[2]	[3]	[4]	[5]	[6]	[7]	[8]	[9]	[10]	[11]
Target	SED class	SpT[a]	T^a	$\dot{M}^d_{\rm acc}$	L^c_*	$L^e_{\rm X}$	$L^d_{\rm acc}$	Age[c]	$M^f_{\rm disc}$	Sep. (pair)[g]
[–]	[–]	[–]	[K]	[10^{-7} $M_\odot$ yr^{-1}]	[$L_\odot$]	[$L_\odot$]	[$L_\odot$]	[Myr]	[$M_\odot$]	[arcsec]
Non-outflows										
DH Tau	II	M2.3	3515	0.77	0.68	8.458	0.05	1.0	0.003	...
DI Tau	III	M0.7	3680	0.01	0.62	1.568	0.001	1.9	...	...
DK Tau	II	K8.5(A)+M1.7(B)	3960(A)+3650(B)	15.40	1.32	0.916	0.98	1.0	0.005	2.30 (A–B)
DM Tau	T	M3	3410	0.09	0.25	...	0.01	2.8	0.02	...
DN Tau	T	M0.3	3830	0.43	0.91	1.155	0.03	0.9	0.03	...
DS Tau	II	M0.4	3860	2.21	0.72	...	0.33	7.8	0.006	...
FF Tau	III	K8	3990	0.02	0.81	0.796	0.002	2.3	...	...
FM Tau	II	M4.5	3100	0.99	0.32	0.532	0.11	4.5	0.002	...
FO Tau	T	M3.9	3190	1.05	0.88	0.065	0.03	0.4	0.0006	0.15 (A–B)
FQ Tau	II	M4.3	3110	0.21	0.32	0.049	0.01	1.7	0.001	0.76 (A–B)
FT Tau	II	M2.8	3430	...	0.38	...	...	...	0.01	...
FW Tau	III	M5.8	2870	...	0.23	...	...	1.2	0.0002	0.08 (A–B)
FX Tau	II	M2.2	3510	0.44	1.02	0.502	0.02	0.5	0.0009	0.89 (A–B)
GH Tau	II	M2.3	3515	...	0.79	0.109	...	0.5	0.0007	0.31 (A–B)
GI/GK Tau	II	M0.4/K6.5(A)	3770/4160(A)	2.96/1.99	0.85/1.17	0.833/1.471	0.31/0.13	3.5/1.4	...	13.15
GM Aur	T	K6	4115	0.60	1.00	...	0.12	9.6	0.03	...
GO Tau	II	M2.3	3515	0.22	0.27	0.249	0.03	5.2	0.07	...
Haro 6–37	II	K8(A)+M0.9(B)	4050(A)+3720(B)	1.41	...	...	...	0.06	0.01	2.62 (A–B)
HBC 347	III	K1	5080[c]	...	...	...	...	...	<0.0004	...
HBC 356	III	K2	4905[c]	...	0.17	...	0.01	...	<0.0004	...
HBC 358	III	M3.9	3200	0.001	0.28	...	0.0001	3.0	<0.0005	...
HD 283572	III	G4	5560	6.12	6.46	13.003[c]	1.16	5.8	...	...
HK Tau	II	M1.5	3670	0.32	0.47	0.079	0.03	2.2	0.004	2.34 (A–B)
HO Tau	II	M3.2	3365	0.10	0.20	0.047	0.02	5.4	0.002	...
IP Tau	T	M0.6	3770	0.06	0.43	...	0.01	3.1	0.03	...
IQ Tau	II	M1.1	3690	0.82	0.65	0.416	0.04	1.4	0.02	...
J1–4872	III	M0.6(A)+M3.7(B)	3770(A)+3250(B)	...	0.72	...	...	2.8	...	3.40 (A–B)
LkCa 1	III	M3.6	3350	...	0.37	0.232	...	0.6	...	...
LkCa 3	III	M2.4	3510	0.01	1.66	...	0.0004	0.2	<0.0004	0.48 (A–B)
LkCa 4	III	M1.3	3680	0.20	0.85	...	0.02	2.2	<0.0002	...
LkCa 5	III	M2.2	3520	...	0.29	0.432	...	1.9	<0.0002	...
LkCa 7	III	M1.2	3680	0.26	0.89	...	0.02	2.1	<0.0004	1.02 (A–B)
LkCa 15	T	K5.5	4190	0.44	0.83	...	0.06	5.2	0.05	...
UX Tau	T	K0(E)+M1.9(W)	4870(E)+3560(W)	1.35	1.30(A)+0.35(B)	...	0.13	8.0(A)+7.5(B)	0.005	5.86 (A–B)
V710 Tau	II	M3.3(A)+M1.7(B)	3350(A)+3650(B)	0.22	0.63(A)+0.36(B)	1.378	0.02	1.8(A)+1.8(B)	0.007	3.17 (A–B)
V807 Tau	II	K7.5	3930	4.26	4.10	1.049	0.27	0.2	...	0.30 (A–B)
V819 Tau	II/III	K8	3990	0.27	0.81	2.205	0.03	2.3	0.0004	...
V836 Tau	T	M0.8	3740	0.1	0.51	...	0.01	7.9	...	...
V927 Tau	III	M4.9	2990	...	0.33	...	...	0.3	<0.0005	0.27 (A–B)
V1096 Tau	III	M0	3850[c]	...	1.30	4.139	...	0.5	<0.0004	...
VY Tau	II	M1.5	3670	0.05	0.42	...	0.01	3.0	<0.0005	0.66 (A–B)
ZZ Tau	II	M4.3	3100	0.04	0.69	...	0.001	0.4	...	...

Appendix B: Observations

Table B.1 shows the complete Taurus GASPS list of observations. The object coordinates, identifiers (OBSIDs) of line (LineSpec) and range (RangeSpec) observing modes along with exposure times are given.

Table B.1. Overview of the spectroscopic OBSIDs that were observed.

Star	RA[h:m:s]	Dec[d:m:s]	LineSpec ID	RangeSpec ID	t_{exp}[s]
AA Tau	04:34:55.42	+24:28:53.20	1342190357	1342190356 (D3)	1252/5141
			1342225758	1342225759 (D3)	6628/20555
BP Tau	04:19:15.83	+29:06:26.90	1342192796		1252
			1342225728		3316
CIDA 2	04:15:05.16	+28:08:46.20	1342216643		1252
CI Tau	04:33:52.00	+22:50:30.20	1342192125	1342192124 (D3)	1252/5141
CW Tau	04:14:17.00	+28:10:57.80	1342216221	1342216222 (D3)	1252/10 279
CX Tau	04:14:47.86	+26:48:11.01	1342225729		3316
CY Tau	04:17:33.73	+28:20:46.90	1342192794		1252
Coku Tau/4	04:41:16.81	+28:40:00.60	1342191360		1252
			1342225837		6628
DE Tau	04:21:55.64	+27:55:06.10	1342192797	1342216648 (D2)	1252/8316
DF Tau	04:27:03.08	+25:42:23.30	1342190359	1342190358 (D3)	1252/5141
DG Tau	04:27:04.70	+26:06:16.30	1342190382	1342190383 (D3)	1252/5141
DG Tau B	04:27:02.56	+26:05:30.70	1342192798	1342216652 (D3)	1252/10 279
DH Tau^{+}	04:29:42.02	+26:32:53.20	1342225734		1252
DK Tau	04:30:44.24	+26:01:24.80	1342192132	1342192133 (D3)	1252/5141
			1342225732		3316
DL Tau	04:33:39.06	+25:20:38.20	1342190355	1342190354 (D3)	1252/5141
			1342225800		6628
DM Tau	04:33:48.72	+18:10:10.00	1342192123	1342192122 (D3)	1252/5141
			1342225825		6628
DN Tau	04:35:27.37	+24:14:58.90	1342192127	1342192126 (D3)	1252/5141
			1342225757		3316
DO Tau	04:38:28.58	+26:10:49.40	1342190385	1342190384 (D3)	1252/5141
				1342225802 (D2)	12516
DP Tau	04:42:37.70	+25:15:37.50	1342191362	1342225827 (D3)	1252/10 279
DQ Tau	04:46:53.05	+17:00:00.02	1342225806	1342225807 (D2)	1252/8316
DS Tau	04:47:48.11	+29:25:14.45	1342225851		3316
FF Tau	04:35:20.90	+22:54:24.20	1342192802		1252
FM Tau	04:14:13.58	+28:12:49.20	1342216218	1342216219 (D3)	1252/10 279
FO Tau	04:14:49.29	+28:12:30.60	1342216645	1342216644 (D2)	1252/8316
FQ Tau	04:19:12.81	+28:29:33.10	1342192795	1342216650 (D2)	1252/8316
FS Tau*	04:22:02.18	+26:57:30.50	1342192791	1342214358 (D3)	1252/10279
FT Tau	04:23:39.19	+24:56:14.10	1342192790	1342243501 (D1)	1252/1637
FW Tau	04:29:29.71	+26:16:53.20	1342225735		1252
FX Tau	04:30:29.61	+24:26:45.00	1342192800		1252
GG Tau	04:32:30.35	+17:31:40.60	1342192121	1342192120 (D3)	1252/5141
				1342225738 (D2)	12 516
GH Tau*	04:33:06.43	+24:09:44.50	1342192801	1342225762 (D2)	1252/8316
GI/K Tau†	04:33:34.31	+24:21:11.50	1342225760		3316
GM Aur	04:55:10.99	+30:21:59.25	1342191357	1342191356 (D3)	1252/5141
GO Tau	04:43:03.09	+25:20:18.80	1342191361		1252
			1342225826		3316
Haro 6–13	04:32:15.41	+24:28:59.70	1342192128	1342192129 (D3)	1252/5141
				1342225761 (D2)	12516
Haro 6–37	04:46:58.98	+17:02:38.20	1342225805		1252
HBC 347	03:29:38.37	+24:30:38.00	1342192136		1252
HBC 356	04:03:13.99	+25:52:59.90	1342214359		1252

Notes. (D) stands for deeper observations than the regular settings. (D1): observations at 72 and 145 μm; (D2): observations at 72, 79, 145, and 158 μm; (D3): observations at 72, 78, 90, 145, 158, and 180 μm. $^{(+)}$ DI Tau was observed in the same FOV as DH Tau. $^{(*)}$ Haro 6–5B was observed in the same FOV as FS Tau. $^{(\star)}$ V807 Tau was observed in the same FOV as GH Tau. $^{(\dagger)}$ HL Tau was observed in the same FOV as XZ Tau. $^{(\ddagger)}$ GI/K Tau were spectroscopically unresolved.

Table B.1. continued.

Star	RA[h:m:s]	Dec[d:m:s]	LineSpec ID	RangeSpec ID	t_{exp}[s]
			1342204134		1252
HBC 358	04:03:50.84	+26:10:53.20	1342214680		1252
			1342204347		1252
HD 283572	04:21:58.85	+28:18:06.64	1342216646		1660
HK Tau	04:31:50.57	+24:24:18.07	1342225736	1342225737 (D2)	3316/8316
HN Tau	04:33:39.35	+17:51:52.37	1342225796	1342225797 (D3)	3316/10 279
HO Tau	04:35:20.20	+22:32:14.60	1342192803		1252
HV Tau	04:38:35.28	+26:10:38.63	1342225801		3316
IP Tau	04:24:57.08	+27:11:56.50	1342225756		3316
IQ Tau	04:29:51.56	+26:06:44.90	1342225733	1342192134 (D3)	3316/5141
			1342192135		1252
IRAS 04158+2805	04:18:58.14	+28:12:23.50	1342192793	1342192792 (D3)	1252/5141
IRAS 04385+2550	04:41:38.82	+25:56:26.75	1342225828	1342225829 (D2)	3316/8316
J1-4872	04:25:17.68	+26:17:50.41	1342216653		1660
LkCa 1	04:13:14.14	+28:19:10.84	1342214679		1660
LkCa 3	04:14:47.97	+27:53:34.65	1342216220		1660
LkCa 4	04:16:28.11	+28:07:35.81	1342216642		1660
LkCa 5	04:17:38.94	+28:33:00.51	1342216641		1660
LkCa 7	04:19:41.27	+27:49:48.49	1342216649		1660
LkCa 15	04:39:17.80	+22:21:03.48	1342190387	1342190386 (D3)	1252/5141
			1342225798		6628
RW Aur	05:07:49.54	+30:24:05.07	1342191359	1342191358 (D3)	1252/5141
RY Tau	04:21:57.40	+28:26:35.54	1342190361	1342190360 (D3)	1252/5141
				1342216647 (D2)	12516
SU Aur	04:55:59.38	+30:34:01.56	1342217844	1342217845 (D3)	3316/10 279
T Tau	04:21:59.43	+19:32:06.37	1342190353	1342190352 (D3)	1252/5141
UX Tau	04:30:03.99	+18:13:49.40	1342214357		1252
			1342204350		1252
UY Aur	04:51:47.38	+30:47:13.50	1342215699	1342226001 (D3)	1252/10 279
			1342193206		1252
UZ Tau	04:32:42.89	+25:52:32.60	1342192131	1342192130 (D3)	1252/5141
V710 Tau	04:31:57.80	+18:21:35.10	1342192804		1252
V773 Tau	04:14:12.92	+28:12:12.45	1342216217		3316
V819 Tau	04:19:26.26	+28:26:14.30	1342216651		1660
V836 Tau	05:03:06.60	+25:23:19.71	1342227634		3316
V927 Tau	04:31:23.82	+24:10:52.93	1342225763		3316
V1096 Tau	04:13:27.23	+28:16:24.80	1342214678		1252
VY Tau	04:39:17.41	+22:47:53.40	1342192989		1252
XZ Tau[‡]	04:31:39.48	+18:13:55.70	1342190351	1342190350 (D3)	1252/5141
ZZ Tau	04:30:51.38	+24:42:22.30	1342192799		1252

Appendix C: Line fluxes

Tables C.1 and C.2 give the aperture corrected line fluxes integrated over one spaxel in the 60–80 μm and 90–180 μm ranges, respectively. The same holds for Tables C.3 and C.4, but for the fluxes integrated over 3×3 spaxels.

Table C.1. Line fluxes for species in the 60–80 μm range integrated over one spaxel.

Target –	SED Class	[OI] 63.18 μm (10^{-16} W/m^2)	o-H_2O 63.32 μm (10^{-16} W/m^2)	CO 72.84 μm (10^{-16} W/m^2)	o-H_2O 78.74 μm (10^{-16} W/m^2)	p-H_2O 78.92 μm (10^{-16} W/m^2)	OH 79.11 μm (10^{-16} W/m^2)	OH 79.18 μm (10^{-16} W/m^2)	CO 79.36 μm (10^{-16} W/m^2)
Outflows									
AA Tau	II	0.119 (0.038)	0.067 (0.021)	<0.032	0.088 (0.013)	<0.040	0.054 (0.013)	0.052 (0.013)	<0.040
CW Tau	II	0.803 (0.054)	<0.119	<0.048	<0.064	0.055 (0.021)	0.074 (0.021)	<0.064	<0.064
DF Tau	II	0.500 (0.071)	<0.136	<0.074	<0.100	<0.100	<0.100	<0.100	<0.100
DG Tau	II	**5.831 (0.152)**	<0.342	0.134 (0.034)	<0.069	<0.069	0.227 (0.025)	0.183 (0.027)	0.058 (0.023)
DG Tau B	I	**3.265 (0.096)**	<0.211	<0.059	<0.069	0.059 (0.024)	0.124 (0.025)	0.086 (0.024)	<0.069
DL Tau	II	0.184 (0.088)	0.079 (0.019)	<0.078	<0.100	<0.100	<0.100	0.052 (0.016)	<0.100
DO Tau	II	0.735 (0.115)	<0.251	<0.058	<0.100	<0.100	0.075 (0.025)	<0.100	<0.100
DP Tau	II	0.848 (0.042)	<0.112	<0.064	0.076 (0.018)	<0.057	0.141 (0.018)	0.170 (0.027)	<0.057
DQ Tau	II	0.274 (0.048)	<0.122	<0.045	<0.059	0.058 (0.020)	<0.059	<0.059	<0.059
FS Tau	II/Flat	**3.725 (0.051)**	0.182 (0.048)	<0.042	0.226 (0.028)	<0.084	0.523 (0.057)	0.339 (0.028)	<0.10
GG Tau	II	0.550 (0.049)	<0.126	<0.034	0.038 (0.016)	<0.048	0.082 (0.016)	0.047 (0.016)	<0.048
Haro 6–5 B	I	0.399 (0.056)	0.139 (0.049)	<0.061	0.109 (0.042)	0.075 (0.030)	<0.106	<0.106	<0.106
Haro 6–13	II	0.573 (0.047)	<0.109	<0.033	0.055 (0.016)	0.041 (0.016)	0.044 (0.016)	0.044 (0.016)	<0.047
HL Tau	I	4.749 (0.198)	0.536 (0.182)	<0.141	0.820 (0.127)	<0.140	0.198 (0.058)	0.150 (0.049)	<0.198
HN Tau	II	0.487 (0.027)	0.053 (0.024)	<0.049	<0.066	<0.066	<0.066	<0.066	<0.066
HV Tau	I?	0.349 (0.039)	<0.075	–	–	–	–	–	–
IRAS 04158+2805	I	0.582 (0.044)	<0.110	<0.074	<0.093	<0.093	<0.093	<0.093	<0.093
IRAS 04385+2550	II	0.649 (0.029)	<0.078	<0.040	0.079 (0.014)	<0.059	<0.059	<0.059	<0.059
RW Aur	II	1.284 (0.058)	<0.117	<0.076	<0.112	<0.112	<0.112	<0.112	<0.112
RY Tau	T?	0.974 (0.057)	0.203 (0.074)	<0.0452	0.134 (0.028)	<0.082	<0.082	<0.082	<0.082
SU Aur	II	**0.833 (0.030)**	<0.083	<0.042	<0.079	<0.079	<0.079	<0.079	<0.079
T Tau	II/I	**82.171 (0.800)**	2.475 (0.670)	1.088 (0.141)	**5.119 (0.085)**	0.990 (0.085)	**12.685 (0.170)**	**8.386 (0.099)**	1.683 (0.240)
UY Aur	II	**1.585 (0.052)**	<0.132	<0.057	0.349 (0.040)	0.100 (0.044)	0.250 (0.044)	0.223 (0.040)	<0.096
UZ Tau	II	0.187 (0.050)	<0.113	<0.051	<0.086	<0.086	<0.086	<0.086	<0.086
V773 Tau	II	0.774 (0.040)	<0.082	–	–	–	–	–	–
XZ Tau	II	**2.409 (0.055)**	0.174 (0.045)	<0.071	0.221 (0.037)	<0.113	0.240 (0.051)	0.144 (0.028)	<0.113
Non-outflows									
BP Tau	II	0.132 (0.041)	0.106 (0.030)	–	–	–	–	–	–
CI Tau	II	0.326 (0.036)	<0.085	<0.076	<0.093	<0.093	<0.093	<0.093	<0.093
CIDA 2	III	<0.110	<0.110	–	–	–	–	–	–
Coku Tau/4	II	0.234 (0.016)	<0.046	–	–	–	–	–	
CX Tau	T	<0.082	<0.082	–	–	–	–	–	–
CY Tau	II	<0.111	<0.111	–	–	–	–	–	–
DE Tau	II	<0.119	<0.119	<0.045	<0.058	<0.058	<0.058	<0.058	<0.058
DH Tau	II	<0.138	<0.138	–	–	–	–	–	–
DI Tau	III	<0.138	<0.138	–	–	–	–	–	–
DK Tau	II	0.162 (0.025)	<0.055	<0.069	<0.099	<0.099	<0.099	<0.099	<0.099
DM Tau	T	0.107 (0.029)	<0.062	<0.078	<0.107	<0.107	<0.107	<0.107	<0.107
DN Tau	T	0.060 (0.020)	<0.062	<0.072	<0.102	<0.102	<0.102	<0.102	<0.102
DS Tau	II	0.085 (0.012)	<0.063	–	–	–	–	–	–
FF Tau	III	<0.100	<0.100	–	–	–	–	–	–
FM Tau	II	<0.117	<0.117	<0.051	<0.071	<0.071	<0.071	<0.071	<0.071
FO Tau	T	<0.120	<0.120	<0.034	<0.052	<0.052	<0.052	<0.052	<0.052
FQ Tau	II	<0.102	<0.102	<0.042	<0.065	<0.065	<0.065	<0.065	<0.065
FT Tau	II	0.123 (0.035)	<0.097	<0.074	–	–	–	–	–
FW Tau	III	<0.096	<0.096	–	–	–	–	–	–

Table C.1. continued.

Target –	SED Class	[OI] 63.18 μm (10^{-16} W/m^2)	o-H_2O 63.32 μm (10^{-16} W/m^2)	CO 72.84 μm (10^{-16} W/m^2)	o-H_2O 78.74 μm (10^{-16} W/m^2)	p-H_2O 78.92 μm (10^{-16} W/m^2)	OH 79.11 μm (10^{-16} W/m^2)	OH 79.18 μm (10^{-16} W/m^2)	CO 79.36 μm (10^{-16} W/m^2)
Non-outflows									
FX Tau	II	<0.129	<0.129	–	–	–	–	–	–
GH Tau	II	<0.090	<0.090	<0.044	<0.085	<0.085	<0.085	<0.085	<0.085
GI/GK Tau	II	0.127 (0.031)	0.069 (0.022)	–	–	–	–	–	–
GM Aur	T	0.241 (0.045)	<0.119	<0.056	<0.105	<0.105	<0.105	<0.105	<0.105
GO Tau	II	<0.068	<0.068	–	–	–	–	–	–
Haro 6–37	II	<0.133	<0.133	–	–	–	–	–	–
HBC 347	III	<0.128	<0.128	–	–	–	–	–	–
HBC 356	III	<0.081	<0.081	–	–	–	–	–	–
HBC 358	III	<0.102	<0.102	–	–	–	–	–	–
HD 283572	III	<0.095	<0.095	–	–	–	–	–	–
HK Tau	II	0.370 (0.032)	<0.090	<0.031	<0.064	<0.064	<0.064	<0.064	<0.064
HO Tau	II	<0.114	<0.114	–	–	–	–	–	–
IP Tau	T	<0.076	<0.076	–	–	–	–	–	–
IQ Tau	II	0.157 (0.025)	0.098 (0.040)	<0.072	<0.117	<0.117	<0.117	<0.117	<0.117
J1–4872	III	<0.119	<0.119	–	–	–	–	–	–
LkCa 1	III	<0.099	<0.099	–	–	–	–	–	–
LkCa 3	III	<0.098	<0.098	–	–	–	–	–	–
LkCa 4	III	<0.103	<0.103	–	–	–	–	–	–
LkCa 5	III	<0.101	<0.101	–	–	–	–	–	–
LkCa 7	III	<0.110	<0.110	–	–	–	–	–	–
LkCa 15	T	0.126 (0.024)	<0.057	<0.078	<0.107	<0.107	<0.107	<0.107	<0.107
UX Tau	T	0.395 (0.035)	<0.095	–	–	–	–	–	–
V710 Tau	II	<0.105	<0.105	–	–	–	–	–	–
V807 Tau	II	0.137 (0.058)	<0.108	<0.042	<0.057	<0.057	<0.057	<0.057	<0.071
V819 Tau	II/III	<0.117	<0.117	–	–	–	–	–	–
V836 Tau	T	<0.074	<0.074	–	–	–	–	–	–
V927 Tau	III	<0.085	<0.085	–	–	–	–	–	–
V1096 Tau	III	<0.128	<0.128	–	–	–	–	–	–
VY Tau	II	<0.097	<0.097	–	–	–	–	–	–
ZZ Tau	II	<0.115	<0.115	–	–	–	–	–	–

Notes. Fluxes in bold text represent misaligned and/or extended sources. In these cases the 3×3 fluxes (see Tables C.3 and C.4) are more accurate and are used in the calculations.

Table C.2. Line fluxes for species in the 90–180 μm range integrated over one spaxel.

Target	SED	p-H_2O 89.99 μm	CO 90.16 μm	p-H_2O 144.52 μm	CO 144.78 μm	[OI] 145.52 μm	[CII] 157.74 μm	o-H_2O 179.53 μm	o-H_2O 180.49 μm
–	Class	(10^{-16} W/m^2)	(10^{-16} W/m^2)	(10^{-16} W/m^2)	(10^{-16} W/m^2)	(10^{-16} W/m^2)	(10^{-16} W/m^2)	(10^{-16} W/m^2)	(10^{-16} W/m^2)
Outflows									
AA Tau	II	<0.033	<0.047	<0.016	0.038 (0.006)	0.009 (0.006)	<0.023	<0.023	<0.023
CW Tau	II	0.045 (0.018)	0.089 (0.027)	<0.030	0.058 (0.010)	<0.030	0.044 (0.012)	<0.028	<0.028
DF Tau	II	<0.071	<0.071	<0.041	<0.041	<0.041	<0.055	<0.061	<0.061
DG Tau	II	0.066 (0.027)	0.096 (0.024)	<0.044	**0.255 (0.014)**	**0.396 (0.014)**	**0.948 (0.014)**	<0.081	<0.081
DG Tau B	I	<0.055	<0.061	0.027 (0.011)	**0.105 (0.011)**	**0.167 (0.011)**	**0.082 (0.016)**‡	<0.040	<0.040
DL Tau	II	0.076 (0.027)	<0.082	<0.045	<0.045	<0.045	<0.054	<0.061	<0.061
DO Tau	II	<0.054	<0.070	<0.034	0.035 (0.011)	0.048 (0.011)	<0.061	<0.081	<0.081
DP Tau	II	<0.057	0.082 (0.018)	0.024 (0.007)	0.081 (0.007)	0.037 (0.007)	0.082 (0.011)‡	<0.037	<0.037
DQ Tau	II	–	–	<0.017	<0.017	<0.017	0.025 (0.009)	–	–
FS Tau	II/Flat	0.056 (0.014)	0.059 (0.017)	<0.035	0.317 (0.011)	0.160 (0.011)	0.157 (0.013)‡	0.325 (0.013)	0.068 (0.013)
GG Tau	II	<0.082	<0.082	<0.023	0.054 (0.007)	0.018 (0.007)	<0.028	<0.056	<0.056
Haro 6–5 B	I	<0.079	<0.079	0.047 (0.011)	0.091 (0.011)	0.038 (0.011)	0.068 (0.013)‡	<0.042	<0.042
Haro 6–13	II	<0.079	<0.079	0.025 (0.007)	0.078 (0.007)	<0.020	<0.031	<0.061	<0.061
HL Tau	I	0.255 (0.042)	0.255 (0.042)	<0.250	0.977 (0.092)	0.864 (0.079)	<0.254	<0.085	<0.085
HN Tau	II	<0.057	<0.057	0.199 (0.006)	<0.017	0.031 (0.006)	<0.028	<0.028	<0.028
IRAS 04158+2805	I	<0.085	<0.085	<0.028	0.042 (0.013)	0.030 (0.013)	<0.062	<0.058	<0.058
IRAS 04385+2550	II	–	–	<0.020	0.0548 (0.007)	0.031 (0.007)	0.024 (0.010)‡	–	–
RW Aur	II	<0.076	<0.076	<0.040	0.148 (0.013)	0.069 (0.013)	<0.055	0.139 (0.020)	<0.059
RY Tau	T?	0.096 (0.028)	0.083	0.037 (0.010)	0.038 (0.010)	0.027 (0.010)	0.038 (0.007)‡	<0.051	<0.051
SU Aur	II	<0.048	<0.049	<0.027	0.038 (0.008)	0.035 (0.008)	0.047 (0.013)‡	<0.031	<0.031
T Tau	II/I	3.408 (0.057)	**3.411 (0.064)**	**0.846 (0.035)**	**7.210 (0.033)**	**3.534 (0.035)**	**1.892 (0.023)**	**3.780 (0.038)**	**1.254 (0.042)**
UY Aur	II	0.098 (0.028)	0.103 (0.023)	0.048 (0.010)	0.254 (0.010)	0.171 (0.010)	**0.151 (0.011)**‡	0.151 (0.010)	<0.031
UZ Tau	II	<0.065	<0.065	<0.044	<0.044	<0.044	<0.051	<0.069	<0.069
XZ Tau	II	0.136 (0.027)	0.045 (0.024)	0.089 (0.013)	**0.311 (0.013)**	0.141 (0.013)	0.225 (0.027)‡	0.168 (0.017)	0.071 (0.023)
Non-outflows									
CI Tau	II	<0.076	<0.107	<0.049	0.041 (0.017)	<0.049	<0.042	<0.051	<0.051
DE Tau	II	–	–	<0.017	0.024 (0.006)	0.016 (0.006)	<0.030	–	–
DK Tau	II	<0.078	<0.078	<0.049	<0.049	<0.0495	<0.065	<0.062	<0.062
DM Tau	T	<0.072	<0.072	<0.042	<0.042	<0.042	<0.047	<0.047	<0.047
DN Tau	T	<0.075	<0.075	<0.033	<0.033	<0.033	<0.042	<0.058	<0.058
FO Tau	T	–	–	<0.020	<0.020	<0.020	<0.023	–	–
FM Tau	II	<0.059	<0.059	<0.025	<0.025	<0.025	<0.044	<0.044	<0.044
FQ Tau	II	–	–	<0.027	<0.027	<0.027	<0.027	–	–
FT Tau	II	–	–	<0.040	<0.040	<0.040	–	–	–
GH Tau	II	–	–	<0.021	<0.021	<0.021	<0.030	–	–
GM Aur	T	<0.085	<0.057	<0.042	<0.042	<0.042	<0.065	<0.058	<0.058
HK Tau	II	–	–	<0.018	0.031 (0.006)	<0.021	<0.021	–	–
IQ Tau	II	<0.079	<0.079	<0.037	<0.037	<0.037	<0.051	<0.040	<0.040
LkCa 15	T	<0.078	<0.078	<0.047	<0.047	<0.047	<0.054	<0.048	<0.048
V807 Tau	II	–	–	<0.028	<0.028	<0.028	<0.028	–	–

Notes. Fluxes in bold text represent misaligned and/or extended sources. In these cases the 3×3 fluxes (see Tables C.3 and C.4) are more accurate and are used in the calculations. (‡) Objects shown in Fig. 14 with [CII] contamination in the *off*-source positions.

Table C.3. Line fluxes for species in the 60–80 μm range integrated over 3 × 3 spaxels.

Target	SED	[OI] 63.18 μm	o-H_2O 63.32 μm	CO 72.84 μm	o-H_2O 78.74 μm	p-H_2O 78.92 μm	OH 79.11 μm	OH 79.18 μm	CO 79.36 μm
–	Class	(10^{-16} W/m^2)	(10^{-16} W/m^2)	(10^{-16} W/m^2)	(10^{-16} W/m^2)	(10^{-16} W/m^2)	(10^{-16} W/m^2)	(10^{-16} W/m^2)	(10^{-16} W/m^2)
Outflows									
AA Tau	II	0.21 (0.06)	<0.18	<0.10	<0.15	<0.15	<0.15	<0.15	<0.15
CW Tau	II	1.09 (0.28)	<0.50	<0.16	<0.25	<0.25	<0.25	<0.25	<0.25
DF Tau	II	<0.53	<0.53	<0.21	<0.36	<0.36	<0.36	<0.36	<0.36
DG Tau	II	16.56 (0.59)	<1.02	<0.20	<0.40	<0.40	<0.40	<0.40	<0.40
DG Tau B	I	6.36 (0.37)	<0.71	<0.17	<0.34	<0.34	<0.34	<0.34	<0.34
DL Tau	II	<0.56	<0.56	<0.26	<0.42	<0.42	<0.42	<0.42	<0.42
DO Tau	II	2.00 (0.47)	<0.56	<0.29	<0.43	<0.43	<0.43	<0.43	<0.43
DP Tau	II	1.37 (0.20)	<0.44	<0.16	<0.27	<0.27	<0.27	<0.27	<0.27
DQ Tau	II	<0.35	<0.35	<0.14	<0.25	<0.25	<0.25	<0.25	<0.25
FS Tau	II/Flat	5.34 (0.19)	<0.43	<0.16	<0.31	<0.31	0.64 (0.20)	0.83 (0.24)	<0.31
GG Tau	II	0.53 (0.12)	<0.34	<0.29	<0.40	<0.40	<0.40	<0.40	<0.40
Haro 6–5B	I	–	–	–	–	–	–	–	–
Haro 6-13	II	0.51 (0.14)	<0.41	<0.27	<0.44	<0.44	<0.44	<0.44	<0.44
HL Tau	I	–	–	–	–	–	–	–	–
HN Tau	II	0.60 (0.09)	<0.23	<0.18	<0.27	<0.27	<0.27	<0.27	<0.27
HV Tau	I?	0.87 (0.18)	<0.31	–	–	–	–	–	–
IRAS 04158+2805	I	0.71 (0.19)	<0.47	<0.21	<0.36	<0.36	<0.36	<0.36	<0.36
IRAS 04385+2550	II	0.77 (0.12)	<0.27	<0.14	<0.26	<0.26	<0.26	<0.26	<0.26
RW Aur	II	2.33 (0.45)	<0.68	<0.19	<0.40	<0.40	<0.40	<0.40	<0.40
RY Tau	T?	0.99 (0.17)	<0.46	<0.25	<0.34	<0.34	<0.34	<0.34	<0.34
SU Aur	II	1.31 (0.12)	<0.27	<0.19	<0.37	<0.37	<0.37	<0.37	<0.37
T Tau	II/I	183.45 (3.87)	<7.85	1.48 (0.29)	6.47 (0.27)	0.65 (0.18)	11.02 (0.26)	12.87 (0.33)	1.95 (0.28)
UY Aur	II	3.65 (0.16)	<0.40	<0.16	0.39 (0.13)	<0.29	<0.29	<0.29	<0.29
UZ Tau	II	<0.48	<0.48	<0.22	<0.47	<0.47	<0.47	<0.47	<0.47
V773 Tau	II	0.91 (0.12)	<0.24	–	–	–	–	–	–
XZ Tau	II	9.63 (0.58)	<1.07	<0.36	<0.75	<0.75	<0.75	<0.75	<0.75
Non-outflows									
BP Tau	II	<0.20	<0.20	–	–	–	–	–	–
CI Tau	II	<0.37	<0.37	<0.26	<0.37	<0.37	<0.37	<0.37	<0.37
CIDA2	III	<0.48	<0.48	–	–	–	–	–	–
CoKuTau/4	II	0.18 (0.04)	<0.17	–	–	–	–	–	–
CX Tau	T	<0.22	<0.22	–	–	–	–	–	–
CY Tau	II	<0.43	<0.43	–	–	–	–	–	–
DE Tau	II	<0.44	<0.44	<0.18	<0.33	<0.33	<0.33	<0.33	<0.33
DH Tau	II	<0.38	<0.38	–	–	–	–	–	–
DI Tau	III	–	–	–	–	–	–	–	–
DK Tau	II	<0.33	<0.33	<0.18	<0.37	<0.37	<0.37	<0.37	<0.37
DM Tau	T	<0.25	<0.25	<0.29	<0.43	<0.43	<0.43	<0.43	<0.43
DN Tau	T	<0.24	<0.24	<0.29	<0.41	<0.41	<0.41	<0.41	<0.41
DS Tau	II	<0.25	<0.25	–	–	–	–	–	–
FF Tau	III	<0.37	<0.37	–	–	–	–	–	–
FM Tau	II	<0.40	<0.40	<0.20	<0.26	<0.26	<0.26	<0.26	<0.26
FO Tau	T	<0.43	<0.43	<0.14	<0.21	<0.21	<0.21	<0.21	<0.21
FQ Tau	II	<0.43	<0.43	<0.15	<0.26	<0.26	<0.26	<0.26	<0.26
FT Tau	II	<0.37	<0.37	<0.26	–	–	–	–	–
FW Tau	III	<0.36	<0.36	–	–	–	–	–	–
FX Tau	II	<0.37	<0.37	–	–	–	–	–	–

Table C.4. Line fluxes for species in the 90–180 μm range integrated over 3 × 3 spaxels.

Target –	SED Class	p-H_2O 89.99 μm (10^{-16} W/m^2)	CO 90.16 μm (10^{-16} W/m^2)	p-H_2O 144.52 μm (10^{-16} W/m^2)	CO 144.78 μm (10^{-16} W/m^2)	[OI] 145.52 μm (10^{-16} W/m^2)	[CII] 157.74 μm (10^{-16} W/m^2)	o-H_2O 179.53 μm (10^{-16} W/m^2)	o-H_2O 180.49 μm (10^{-16} W/m^2)
Outflows									
AA Tau	II	<0.14	<0.14	<0.05	<0.04	<0.05	<0.07	<0.08	<0.08
CW Tau	II	<0.19	<0.19	<0.07	<0.07	<0.07	<0.10	<0.08	<0.08
DF Tau	II	<0.27	<0.27	<0.15	<0.15	<0.15	<0.17	<0.13	<0.13
DG Tau	II	<0.35	<0.35	<0.11	0.60 (0.04)	0.98 (0.04)	2.87(0.09)	<0.20	<0.20
DG Tau B	I	<0.22	<0.22	<0.11	0.26 (0.04)	0.35 (0.04)	0.25 (0.04)	<0.12	<0.12
DL Tau	II	<0.31	<0.31	<0.12	<0.12	<0.12	<0.18	<0.20	<0.20
DO Tau	II	<0.34	<0.34	<0.14	<0.14	<0.14	<0.13	<0.21	<0.21
DP Tau	II	<0.26	<0.26	<0.11	<0.11	<0.11	–	–	–
DQ Tau	II	–	–	<0.07	<0.07	<0.07	<0.08	–	–
FS Tau	II/Flat	<0.20	<0.20	<0.07	0.20 (0.03)	0.14 (0.03)	0.22 (0.04)	<0.11	<0.11
GG Tau	II	<0.38	<0.38	<0.07	0.14(0.05)	<0.07	<0.07	<0.17	<0.17
Haro 6–5 B	I	–	–	–	–	–	–	–	–
Haro 6-13	II	<0.25	<0.25	<0.13	<0.13	<0.13	<0.12	<0.17	<0.17
HL Tau	I	–	–	–	–	–	–	–	–
HV Tau	II	–	–	–	–	–	–	–	–
HN Tau	II	<0.17	<0.17	<0.10	<0.10	<0.10	<0.11	<0.13	<0.13
IRAS 04158+2805	I	<0.28	<0.28	<0.14	<0.14	<0.14	<0.19	<0.18	<0.18
IRAS 04385+2550	II	–	–	<0.08	<0.0	<0.08	<0.10	–	–
RW Aur	II	<0.34	<0.34	<0.10	0.17(0.05)	<0.10	<0.14	<0.18	<0.18
RY Tau	T?	<0.31	<0.31	<0.13	<0.13	<0.13	<0.13	<0.14	<0.14
SU Aur	II	<0.20	<0.20	<0.09	<0.09	<0.09	<0.08	<0.11	<0.11
T Tau	II/I	3.89 (0.17)	4.24 (0.15)	1.28 (0.13)	11.93 (0.12)	7.93 (0.13)	5.65 (0.17)	6.35 (0.12)	2.05 (0.14)
UY Aur	II	<0.25	<0.25	<0.12	0.25 (0.04)	0.17 (0.05)	0.31 (0.05)	0.14 (0.05)	<0.14
UZ Tau	II	<0.27	<0.27	<0.12	<0.12	<0.12	<0.14	<0.22	<0.22
V773 Tau	II	–	–	–	–	–	–	–	–
XZ Tau	II	<0.46	<0.46	<0.31	1.27 (0.11)	0.43 (0.10)	0.43 (0.11)	<0.27	<0.27
Non-outflows									
CI Tau	II	<0.33	<0.33	<0.09	<0.09	<0.09	<0.17	<0.21	<0.21
DE Tau	II	–	–	<0.08	<0.08	<0.08	<0.11	–	–
DK Tau	II	<0.34	<0.34	–	–	–	–	–	–
DM Tau	T	<0.25	<0.25	<0.12	<0.12	<0.12	<0.18	<0.16	<0.16
DN Tau	T	<0.35	<0.35	<0.13	<0.13	<0.13	<0.19	<0.16	<0.16
FO Tau	T	–	–	–	–	–	–	–	–
FM Tau	II	<0.24	<0.24	<0.07	<0.07	<0.07	<0.12	<0.13	<0.13
FQ Tau	II	–	–	<0.09	<0.09	<0.09	<0.08	–	–
FT Tau	II	–	–	<0.14	<0.14	<0.14	–	–	–
GH Tau	II	–	–	<0.10	<0.10	<0.10	<0.12	–	–
GM Aur	T	<0.30	<0.30	<0.14	<0.14	<0.14	<0.17	<0.21	<0.21
HK Tau	II	–	–	<0.07	<0.07	<0.07	<0.10	–	–
IQ Tau	II	<0.42	<0.42	<0.12	<0.12	<0.12	<0.21	<0.17	<0.17
LkCa 15	T	<0.31	<0.31	<0.09	<0.09	<0.09	<0.17	<0.19	<0.19

Appendix D: Detection fractions

Tables D.1–D.3 show respectively the detection fractions statistics in terms of outflow/non-outflow, SED classes and spectral types.

Table D.1. Detection fractions for the entire sample, outflow sources only, and non-outflow sources only.

Species	$\lambda(\mu m)$	All	Outflow	Non-outflow
		Atomic		
[OI]	63.18	55^{+5}_{-6}%(42/76)	100^{+1}_{-6}%(27/27)	31^{+7}_{-6}%(15/49)
[OI]	145.53	49^{+8}_{-8}%(19/39)	75^{+7}_{-11}%(18/24)	7^{+12}_{-2}%(1/15)*
[CII]	157.74	34^{+8}_{-7}%(13/38)	54^{+9}_{-10}%(13/24)	–(0/14)†
		Molecular		
o-H_2O	63.32	17^{+5}_{-3}%(13/76)	37^{+10}_{-8}%(10/27)	6^{+5}_{-2}%(3/49)‡
o-H_2O	78.74	32^{+8}_{-6}%(12/38)	50^{+10}_{-10}%(12/24)	–(0/14)
o-H_2O	179.53	17^{+9}_{-5}%(5/30)	23^{+11}_{-6}%(5/22)	–(0/8)
o-H_2O	180.49	10^{+8}_{-3}%(3/30)	14^{+10}_{-4}%(3/22)	–(0/8)
p-H_2O	78.92	18^{+8}_{-5}%(7/38)	29^{+11}_{-7}%(7/24)	–(0/14)
p-H_2O	89.99	30^{+9}_{-7}%(9/30)	41^{+11}_{-9}%(9/22)	–(0/8)
p-H_2O	144.52	23^{+8}_{-5}%(9/39)	38^{+10}_{-9}%(9/24)	–(0/15)
CO	72.84	5^{+6}_{-2}%(2/39)	8^{+9}_{-3}%(2/24)	–(0/15)
CO	79.36	5^{+6}_{-2}%(2/38)	8^{+9}_{-3}%(2/24)	–(0/14)
CO	90.16	27^{+9}_{-6}%(8/30)	36^{+11}_{-9}%(8/22)	–(0/8)
CO	144.78	56^{+7}_{-8}%(22/39)	79^{+6}_{-10}%(19/24)	20^{+14}_{-7}%(3/15)
OH	79.11	34^{+8}_{-7}%(13/38)	54^{+9}_{-10}%(13/24)	–(0/14)
OH	79.18	32^{+8}_{-6}%(12/38)	50^{+10}_{-10}%(12/24)	–(0/14)

Notes. $^{(\star)}$ Detections in DE Tau. $^{(\ddagger)}$ Detections in: BP Tau (deeper observations), GI/GK Tau (GK Tau is outflow GI Tau is not), IQ Tau. The parentheses indicate the ratio of targets where a certain line is detected over the total number of targets observed. The hyphens mean no detections.

Table D.2. Detection fractions in terms of SED Class.

Species	$\lambda(\mu m)$	Class I	Class II	Class TD	Class III
		Atomic			
[OI]	63.18	100^{+3}_{-26}%(5/5)	70^{+6}_{-8}%(31/44)	60^{+12}_{-16}%(6/10)	–(0/17)
[OI]	145.53	100^{+3}_{-31}%(4/4)	48^{+9}_{-9}%(14/29)	17^{+23}_{-6}%(1/6)	
[CII]	157.74	50^{+20}_{-20}%(2/4)	36^{+10}_{-8}%(10/28)	17^{+23}_{-6}%(1/6)	
		Molecular			
o-H_2O	63.32	40^{+21}_{-16}%(2/5)	23^{+7}_{-5}%(10/44)	10^{+17}_{-3}%(1/10)	–(0/17)
o-H_2O	78.74	50^{+20}_{-20}%(2/4)	32^{+10}_{-7}%(9/28)	17^{+23}_{-6}%(1/6)	
o-H_2O	179.53	–(0/4)	24^{+11}_{-7}%(5/21)	–(0/5)	
o-H_2O	180.49	–(0/4)	14^{+11}_{-5}%(3/21)	–(0/5)	
p-H_2O	78.92	50^{+20}_{-20}%(2/4)	18^{+9}_{-5}%(5/28)	–(0/6)	
p-H_2O	89.99	25^{+27}_{-10}%(1/4)	33^{+11}_{-8}%(7/21)	20^{+25}_{-8}%(1/5)	
p-H_2O	144.52	50^{+20}_{-20}%(2/4)	21^{+9}_{-5}%(6/29)	17^{+23}_{-6}%(1/6)	
CO	72.84	–(0/4)	7^{+8}_{-2}%(2/29)	–(0/6)	
CO	79.36	–(0/4)	7^{+8}_{-2}%(2/28)	–(0/6)	
CO	90.16	25^{+27}_{-10}%(1/4)	33^{+11}_{-8}%(7/21)	–(0/5)	
CO	144.78	100^{+3}_{-31}%(4/4)	59^{+8}_{-9}%(17/29)	17^{+23}_{-6}%(1/6)	
OH	79.11	50^{+20}_{-20}%(2/4)	39^{+10}_{-8}%(11/28)	–(0/6)	
OH	79.18	50^{+20}_{-20}%(2/4)	36^{+10}_{-8}%(10/28)	–(0/6)	

Table D.3. Detection fractions in terms of SpT.

Species	$\lambda(\mu m)$	G0-K7	K7-M1	M1-M3	M3-M6
			Atomic		
[OI]	63.18	84^{+5}_{-12}%(16/19)	61^{+10}_{-12}%(11/18)	35^{+12}_{-9}%(7/20)	42^{+11}_{-10}%(8/19)
[OI]	145.53	62^{+11}_{-14}%(8/13)	50^{+16}_{-16}%(4/8)	38^{+18}_{-13}%(3/8)	40^{+16}_{-12}%(4/10)
[CII]	157.74	46^{+13}_{-12}%(6/13)	25^{+19}_{-9}%(2/8)	25^{+19}_{-9}%(2/8)	33^{+17}_{-11}%(3/9)
			Molecular		
o-H_2O	63.32	32^{+12}_{-8}%(6/19)	17^{+12}_{-5}%(3/18)	10^{+11}_{-3}%(2/20)	11^{+11}_{-4}%(2/19)
o-H_2O	78.74	31^{+15}_{-9}%(4/13)	38^{+18}_{-13}%(3/8)	38^{+18}_{-13}%(3/8)	22^{+18}_{-8}%(2/9)
o-H_2O	179.53	23^{+15}_{-8}%(3/13)	–(0/5)	20^{+25}_{-8}%(1/5)	14^{+21}_{-5}%(1/7)
o-H_2O	180.49	8^{+14}_{-3}%(1/13)	–(0/5)	20^{+25}_{-8}%(1/5)	14^{+21}_{-5}%(1/7)
p-H_2O	78.92	23^{+15}_{-8}%(3/13)	13^{+20}_{-4}%(1/8)	13^{+20}_{-4}%(1/8)	22^{+18}_{-8}%(2/9)
p-H_2O	89.99	54^{+12}_{-13}%(7/13)	–(0/5)	20^{+25}_{-8}%(1/5)	14^{+21}_{-5}%(1/7)
p-H_2O	144.52	31^{+15}_{-9}%(4/13)	–(0/8)	25^{+19}_{-9}%(2/8)	30^{+17}_{-10}%(3/10)
CO	72.84	15^{+15}_{-5}%(2/13)	–(0/8)	–(0/8)	–(0/10)
CO	79.36	15^{+15}_{-5}%(2/13)	–(0/8)	–(0/8)	–(0/9)
CO	90.16	38^{+14}_{-11}%(5/13)	–(0/5)	40^{+21}_{-16}%(2/5)	14^{+21}_{-5}%(1/7)
CO	144.78	69^{+9}_{-15}%(9/13)	50^{+16}_{-16}%(4/8)	63^{+13}_{-18}%(5/8)	40^{+16}_{-12}%(4/10)
OH	79.11	38^{+14}_{-11}%(5/13)	38^{+18}_{-13}%(3/8)	38^{+18}_{-13}%(3/8)	22^{+18}_{-8}%(2/9)
OH	79.18	38^{+14}_{-11}%(5/13)	25^{+19}_{-9}%(2/8)	38^{+18}_{-13}%(3/8)	22^{+18}_{-8}%(2/9)

Appendix E: Diameter of emitting regions

As shown in Flower & Pineau Des Forêts (2010), the relation between the emergent flux, F_e, in erg cm^{-2} s^{-1} and TdV in K km s^{-1} is

$$F_e = \frac{8 \times 10^5 \pi k_B}{\lambda^3} TdV, \quad \text{(E.1)}$$

where λ is the wavelength of the transition in cm, and TdV as provided in Flower & Pineau des Forêts (2015).

The flux observed at the Earth, F_0, then is

$$F_0 = \frac{F_e \Omega}{4\pi}, \quad \text{(E.2)}$$

where Ω str is the solid angle subtended by the source. Given that $\Omega \sim D^2/r^2$, where r and D are the distance to the source and the diameter of the emitting area in au, respectively, then

$$D \sim \sqrt{\frac{4\pi r^2 F_0}{F_e}}. \quad \text{(E.3)}$$

The diameter of the emitting regions provided (see Table 4) are inferred using only the brightest lines among the ratios (i.e. o-H_2O 78.74 μm, CO 144.78 μm, and OH 79.12 μm), besides being compatible with the shock velocities (V_{shock}) and pre-shock densities (n) observed in Figs. E.1–E.4.

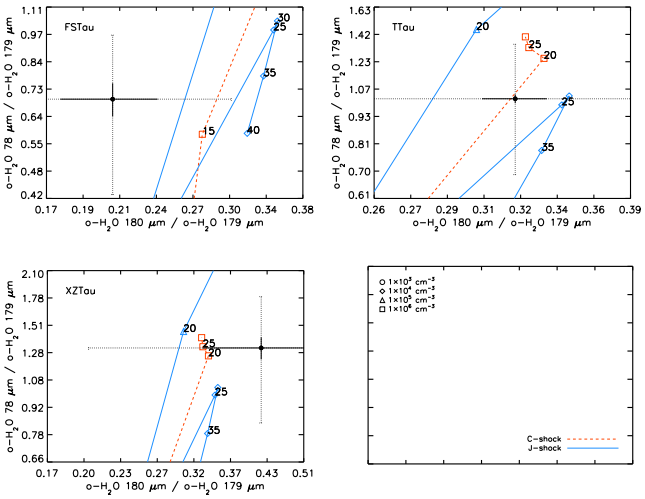

Fig. E.1. Detail of the observed o-H_2O molecular line ratios (78/179 and 180/179) compared to J-type (blue) and C-type (red) shock models from Flower & Pineau des Forêts (2015) for individual sources. The numbers refer to shock velocities (V_{shock}). Different symbols refer to pre-shock densities (n). See legend for details.

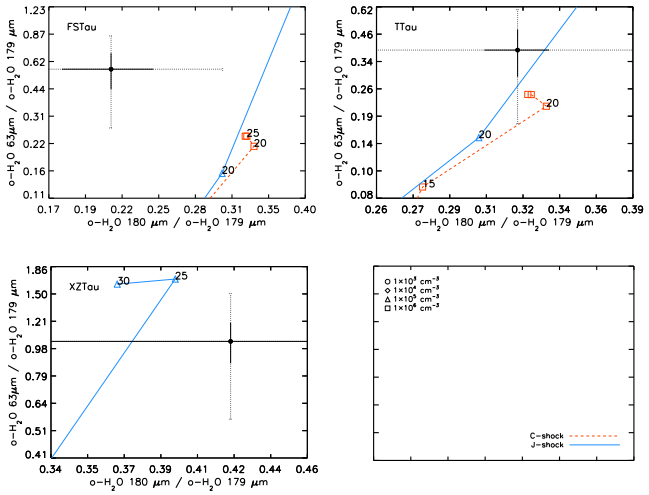

Fig. E.2. Same as Fig. E.1, but for CO and o-H_2O/CO ratios.

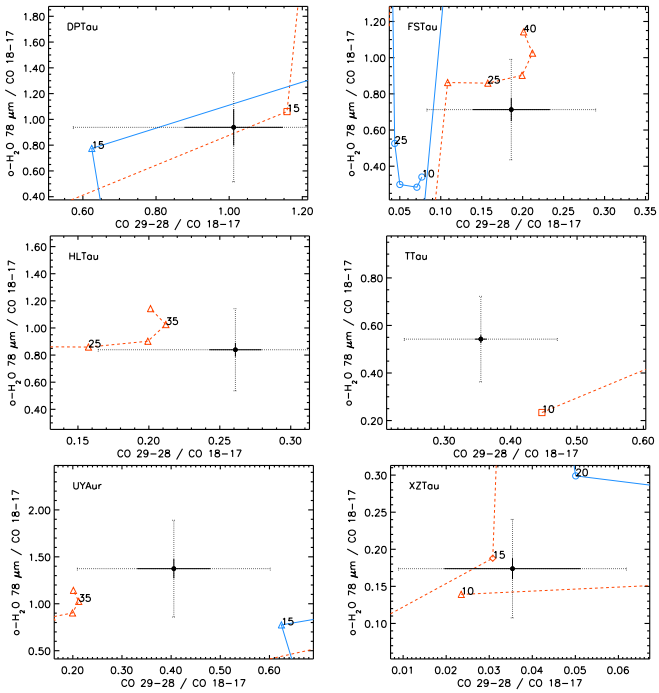

Fig. E.3. Same as Fig. E.1, but for CO and o-H_2O/CO line ratios.

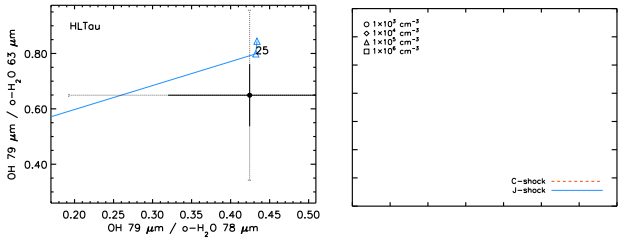

Fig. E.4. Same as Fig. E.1, but for OH/o-H_2O line ratios.

Appendix F: Spectra 60–190 μm

Figures F.1 to F.7 show the objects in the sample with detections in the range 60–190 μm.

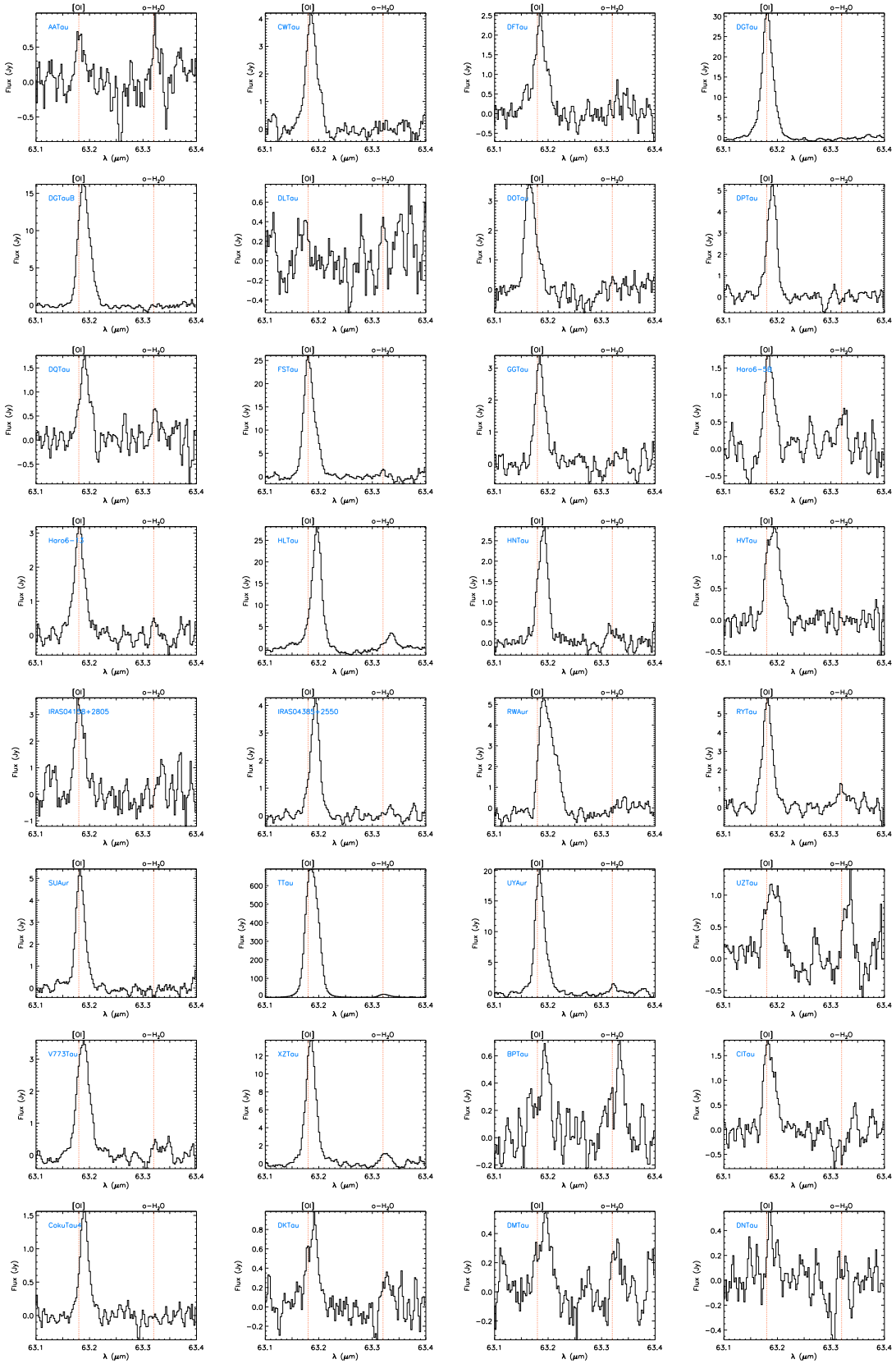

Fig. F.1. Continuum subtracted spectra at 63 μm for all objects with [OI] detections. The red vertical lines indicate the positions of [OI] 63.18 μm and o-H_2O 63.32 μm. The source GI/GK Tau is counted twice to make a total of 42 [OI] detections.

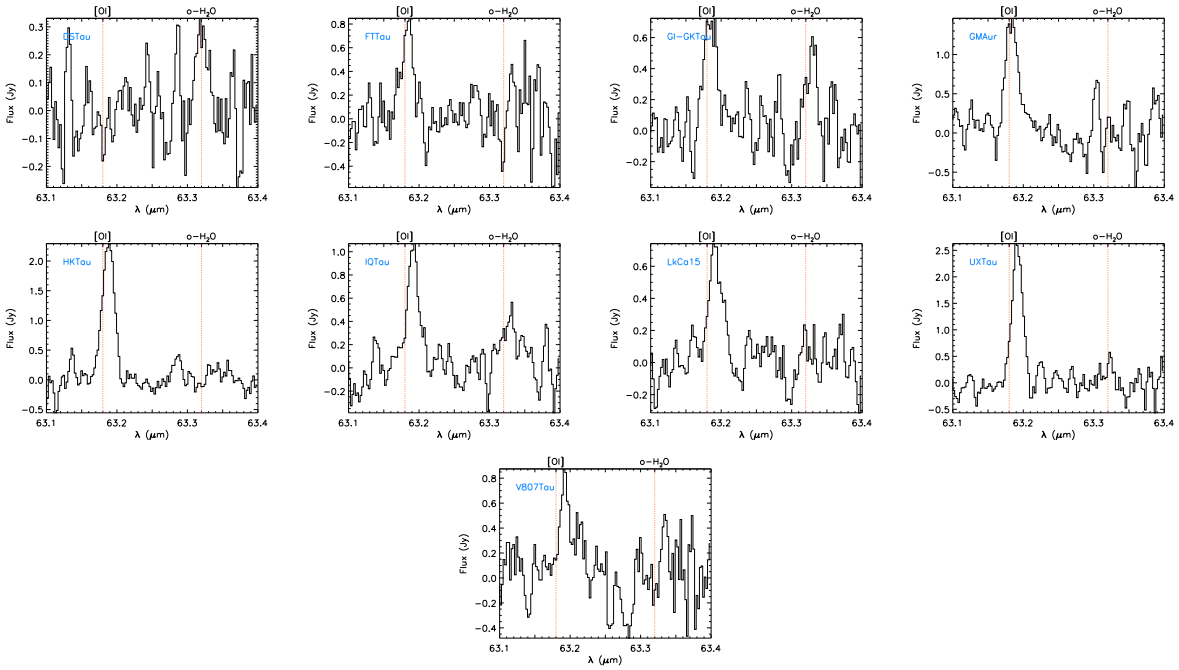

Fig. F.1. continued.

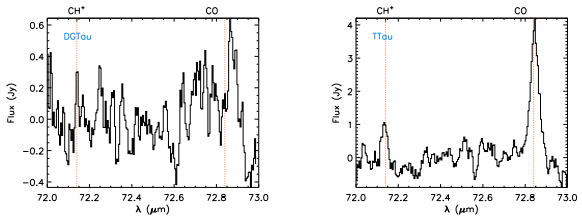

Fig. F.2. Continuum subtracted spectra at 72 μm for all objects with CO detections. The red vertical lines indicate the positions of CH^+ 72.14 μm and CO 72.84 μm.

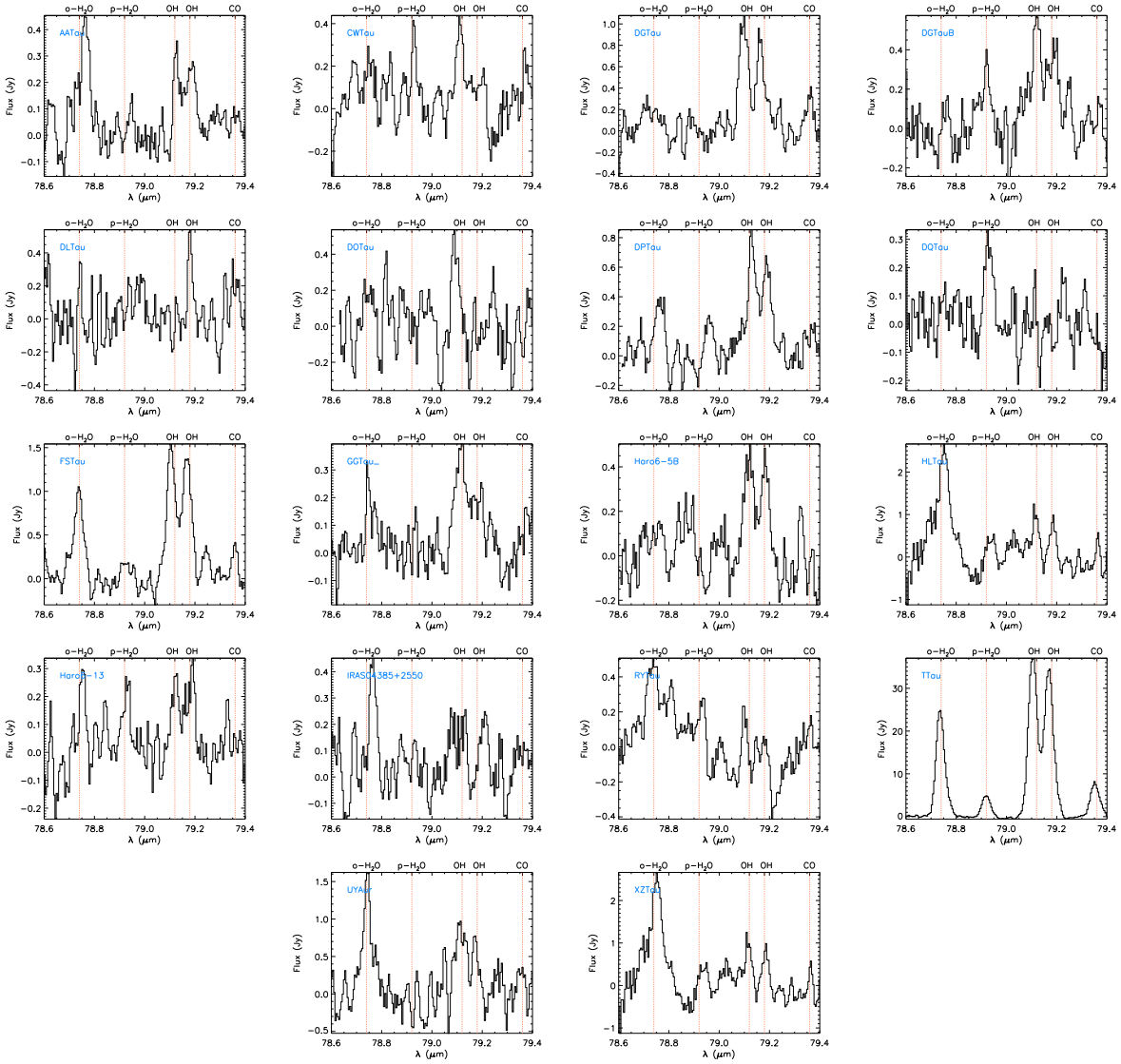

Fig. F.3. Continuum subtracted spectra at 78 μm for all objects with detections. The red vertical lines indicate the positions of o-H_2O 78.74 μm, p-H_2O 78.92 μm, OH 78.12+78.18 μm, and CO 79.36 μm.

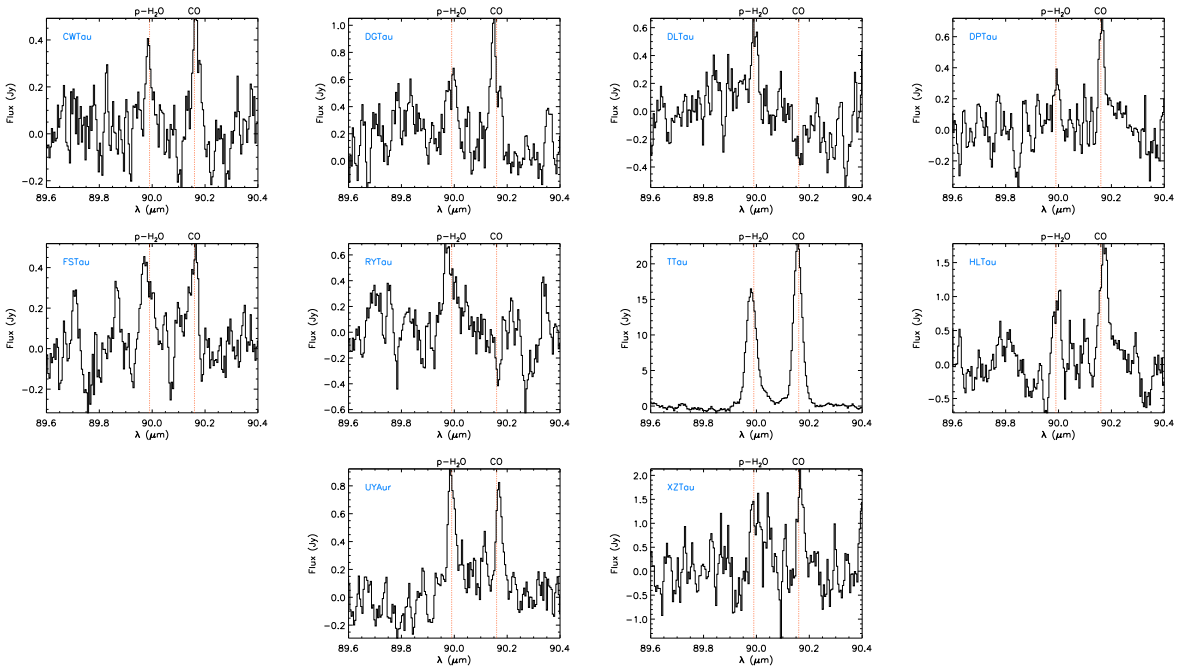

Fig. F.4. Continuum subtracted spectra at 90 μm for all objects with detections. The red vertical lines indicate the positions of p-H_2O 89.99 μm and CO 90.16 μm.

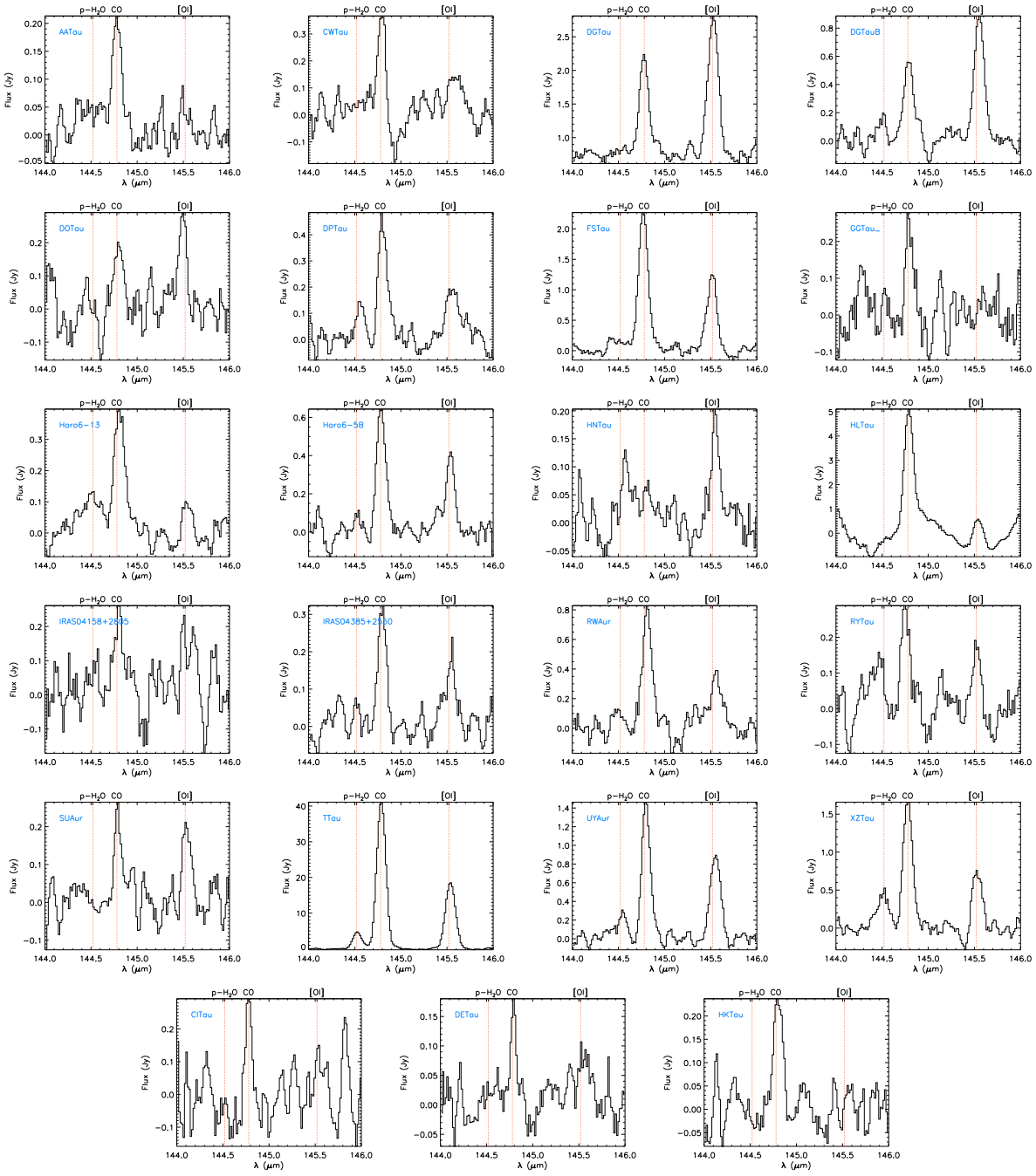

Fig. F.5. Continuum subtracted spectra at 145 μm for all objects with detections. The red vertical lines indicate the positions of p-H_2O 144.52 μm, CO 144.78 μm, and [OI] 145.52 μm.

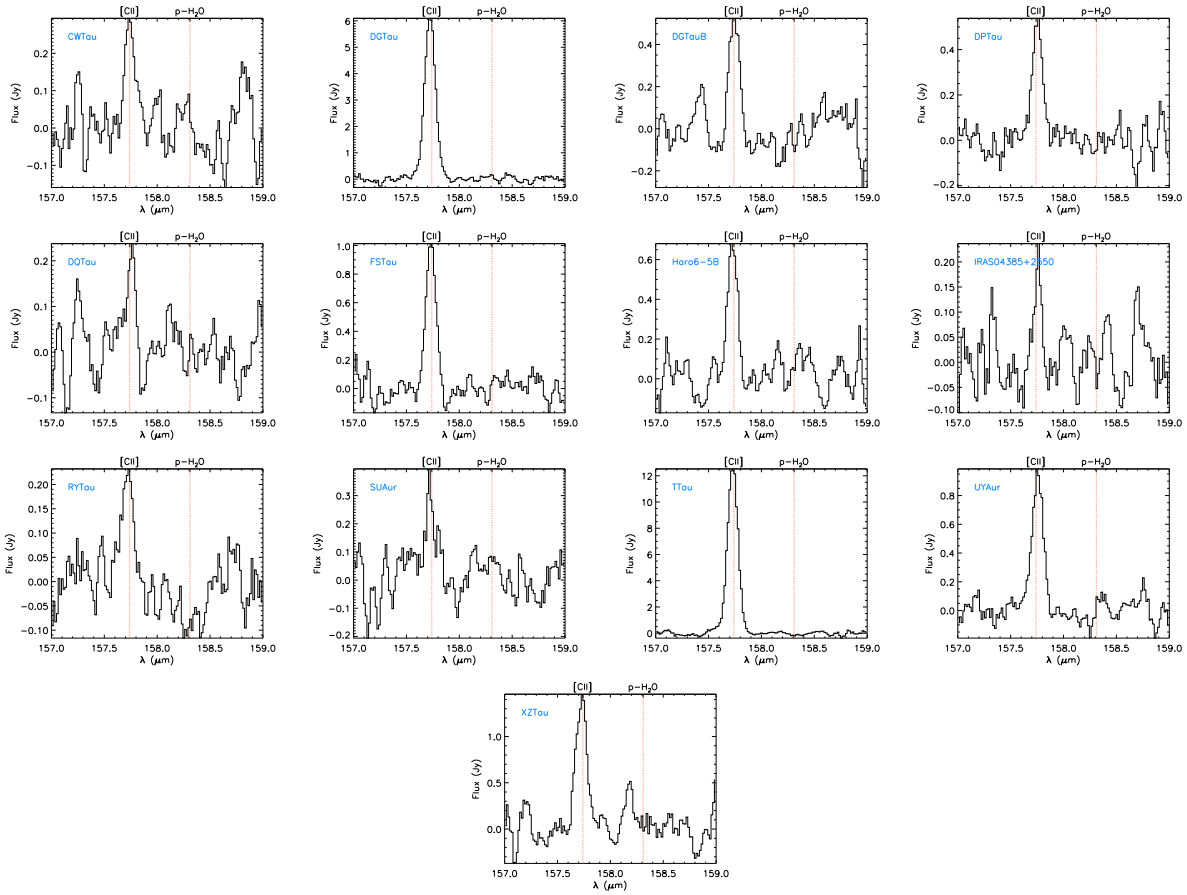

Fig. F.6. Continuum subtracted spectra at 145 μm for all objects with detections. The red vertical lines indicate the positions of [CII] 157.74 μm and p-H_2O 158.31 μm.

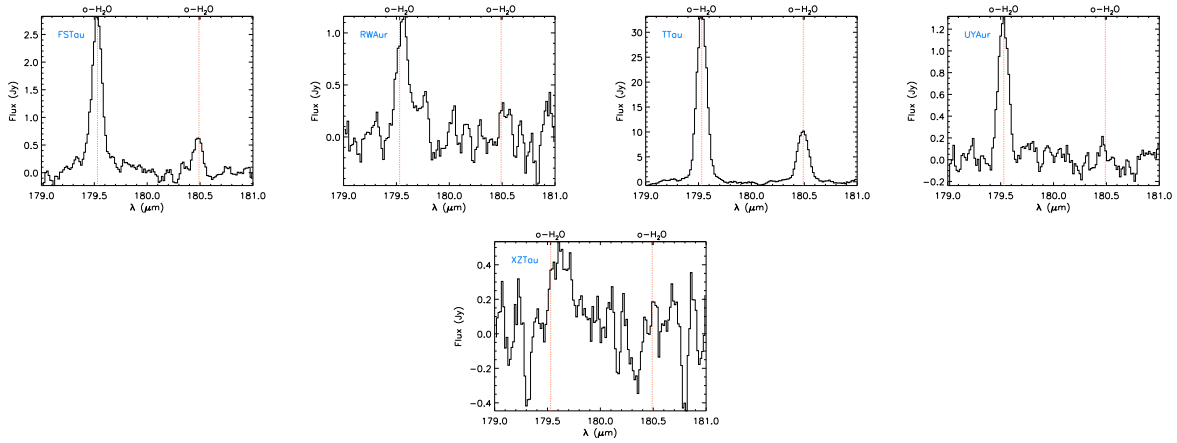

Fig. F.7. Continuum subtracted spectra at 180 μm for all objects with detections. The red vertical lines indicate the positions of o-H_2O 179.53 μm and o-H_2O 180.49 μm.